From mountain range to flat plateau in the Qiangtang Block: Insights from low-temperature thermochronology

Lin Gong[1,8], Qiang Wang[1,2*], Zheng-Xiang Li[3,4], Andrew C. Kerr[5], Xiu-Zheng Zhang[1], Yue Qi[1], Xiao-Ming Shen[6], Zhi-Yong Zhang[7], Bing Chen[1], and Zhi-Wei Yu[1]

1 State Key Laboratory of Deep Earth Processes and Resources, Guangzhou Institute of Geochemistry, Chinese Academy of Sciences, Guangzhou 510640, China

2 College of Earth and Planetary Sciences, University of Chinese Academy of Sciences, Beijing 100049, China

3 Earth Evolution and Dynamics Research Centre, Laoshan Laboratory, Qingdao 266237, China

4 Earth Dynamics Research Group, School of Earth and Planetary Sciences, Curtin University, Perth, WA 6845, Australia

5 School of Earth and Environmental Sciences, Cardiff University, Cardiff CF10 3AT, UK

6 National Institute of Natural Hazards, Ministry of Emergency Management of China, Beijing 100085, China

7 Institute of Geology and Geophysics, Chinese Academy of Sciences, Beijing 100029, China

8 School of Earth Sciences, Yunnan University, Kunming 650500, China

*Corresponding author at: State Key Laboratory of Deep Earth Processes and Resources, Guangzhou Institute of Geochemistry (GIG), Chinese Academy of Sciences (CAS), Wushan Street, Guangzhou 510640, China.

E-mail address: wqiang@gig.ac.cn (Q. Wang).

ABSTRACT

The Tibetan Plateau is currently undergoing lateral extrusion and expansion, but it remains unclear whether such orogen-parallel growth occurred during the Plateau's early uplift. Additionally, it is uncertain how this process developed after the formation of the proto-Tibetan Plateau. Constraining both these processes will help our understanding of the Plateau's uplift history and mechanisms of formation. This study focusses on the Qiangtang terrane, the core of the proto-Tibetan Plateau, and integrates new low-temperature thermochronological data from Eocene granites with published datasets to reconstruct the uplift history from the perspective of spatiotemporal exhumation patterns. Results reveal that prior to 40–35 Ma, the Qiangtang experienced not only orogen-perpendicular growth but also E-W-trending expansion. Following establishment of this proto-Tibetan Plateau, localized exhumation persisted in the North Qiangtang. Combining the correlation between apparent exhumation rate and faults, geomorphic indices, precipitation, and magmatism, we suggest that compressive thickening is the major mechanism that governed the initial uplift, and crustal channel flow induced the northeastward expansion of the Qiangtang Plateau. Conversely, extensional lithosphere thinning, and climate-related erosion processes may only play a role in localized regions. This study reconstructs the uplift history of the Qiangtang Plateau, from its initial formation as a mountain range to a flat plateau. The findings confirm that lateral growth was likely prevalent during the early stage of uplift and provide thermochronological evidence supporting the topographic transition driven by crustal melting.

INTRODUCTION

Most models interpret the Tibetan Plateau's differential uplift as primarily perpendicular to its orogenic belts, consistent with the accretion of serval E-W-trending terranes (Fig. 1A-G; Ding et al., 2022). This lateral growth did not commence until the Miocene, when the plateau was substantially uplifted, especially in southeastern Tibet (Clark and Royden, 2000). Recent paleoelevation data from Cenozoic basins in central-north Tibet have significantly enhanced our understanding of the uplift history of the Tibetan Plateau (Fig. 1H; e.g., Xiong et al., 2022; Li and Garzione, 2023). These data suggest that the Qiangtang Plateau initially uplifted as a mountain range before transitioning into a flat plateau, potentially due to crustal melting (Zhang et al., 2022). However, whether this linear mountain range experienced lateral growth during early uplift, and whether surface exhumation accompanied the crust melting, remains unresolved.

The mechanisms proposed for the formation of the Tibetan Plateau include compressive thickening (e.g., Tapponnier et al., 2001), lithospheric thinning (e.g., Turner et al., 1993; Wang et al., 2022), crustal channel flow (e.g., Clark and Royden, 2000), and climate-induced erosion processes (e.g., Molnar and England, 1990). The uplift of the plateau is generally associated with surface exhumation that can be recorded by thermochronology data, and therefore, the spatiotemporal variations in exhumation rates can provide valuable insights into the uplift processes and geodynamic mechanisms of the plateau (Fig. 2; van der Beek et al., 2009; Rohrmann

et al., 2012; Li et al., 2016; Yin et al., 2023). For instance, if the plateau undergoes uplift due to compressive thickening, exhumation would propagate along with the trend of deformation and thickening (Fig. 2B).

The existing thermochronologic data from Qiangtang indicate that negligible exhumation has occurred since ca. 45-40 Ma (Wang et al., 2008a; Rohrmann et al., 2012). However, as most of these data are derived from pre-Cenozoic bedrock and sedimentary rocks, it remains unclear whether younger (< 40 Ma) cooling events have taken place. In this study we report comprehensive low-temperature thermochronology on the Eocene granites from the Qiangtang Plateau to assess whether significant exhumation occurred since their emplacement. The compiled data were then combined to determine the tempo-spatial variations in exhumation rate. Finally, the varying patterns of apparent exhumation and its relation to faults, geomorphic indices (e.g., slope, relief), precipitation, and magmatism were employed to assess the growth history of the Qiangtang Plateau and its formation mechanisms.

GEOLOGICAL SETTING

The Qiangtang (QT) Plateau is located in the central Tibetan Plateau and is bordered by the Bangong-Nujiang suture to the south and the Jinsha suture to the north (Fig. 2A; Ding et al., 2022). Tectonically, the Qiangtang can be divided into southern Qiangtang (SQT) and northern Qiangtang (NQT) by the Longmu Co-Shuanghu suture (Li et al., 2009). This suture zone comprises a suite of high-pressure metamorphic rocks, such as eclogite, blueschist, and

garnet-phengite-quartz schist (Dan et al., 2025). Although some early studies interpreted the high-pressure metamorphic rocks along the Longmu Co-Shuanghu belt as underplated mélange resulting from the southward subduction of the Songpan-Ganzi oceanic lithosphere (e.g., Kapp et al., 2000), most recent research supports the interpretation that the Longmu Co-Shuanghu suture zone marks the closure of the Paleo-Tethys Ocean and the subsequent collision between the South Qiangtang (SQT) and the North Qiangtang (NQT) terranes at ca. 235 Ma (Li et al., 2009; Dan et al., 2025; Xu et al., 2025). Following the amalgamation of the SQT and NQT, the Qiangtang terrane experienced widespread marine sedimentation during the Late Triassic to Early Cretaceous (Li et al., 2025). These marine strata were subsequently unconformably overlain by sparse terrestrial deposits during the Late Cretaceous to Eocene (Kapp et al., 2005; Bi et al., 2023).

Since the Cretaceous, a series of E-W–trending folds and thrust faults have deformed and shortened the Qiangtang terrane, including the Fenghuoshan, Tanggula, Lugu-Rongma, Zadaona-Riganpei Co, Gangma Co-Shuanghu, Southern Qiangtang, Shiquanhe-Gaize-Amdo, and Gaize-Siling Co thrust belts (Kapp et al., 2005, 2007; Li et al., 2015; Staisch et al., 2016). These structures not only contributed to the uplift of the Qiangtang Plateau but also played a dominant role in shaping the adjacent Cenozoic basins (Xue et al., 2022; Bi et al., 2023). Since the Miocene, a series of N–S-trending rifts and normal faults have developed across the Qiangtang Plateau, including the Shuanghu Rift, Yibug Caka Fault, and Mugs Purou Fault (Blisniuk et al., 2001; Li et al., 2015).

Cenozoic magmatic rocks are widely distributed across the Qiangtang Plateau and can be classified into four distinct magmatic episodes: 46–38 Ma and 6.8–2.3 Ma in the Northern Qiangtang (NQT), 37–34 Ma in the Southern Qiangtang (SQT), and 31–28 Ma in the western Qiangtang (QT) (Qi et al., 2024). Most of these magmatic rocks are volcanic, comprising basanite/tephrite, trachyte, trachybasalt, phonolite, trachyandesite, basalt, and dacite (Ou et al., 2019; Qi et al., 2023, 2024; Liu et al., 2024). Additionally, minor Eocene (42–37 Ma) granitoids are sporadically distributed along the Tanggula range in the NQT, including the Puruo Gangri, Geladandong, Saiduopu Gangri, Meiriqie Co, Qoima Co, Dushan, and Maliaoshan plutons (Ou et al., 2017; Liu et al., 2022; Xu et al., 2022).

Low-temperature thermochronological work on pre-Cenozoic rocks across the Qiangtang Plateau indicate that most regions have undergone little to no significant exhumation since ca. 45–40 Ma (Wang et al., 2008a; Rohrmann et al., 2012; Dai et al., 2013). The initial cooling and exhumation history of the Qiangtang Plateau is well constrained by bedrock thermochronology data from the Central Qiangtang Mountain Range, which reveals a period of rapid cooling during the Middle Jurassic to Cretaceous (Zhao et al., 2017; Qian et al., 2021; Zhao et al., 2022). This cooling event has been interpreted as being linked to the collision between the Qiangtang and Lhasa terranes (Zhao et al., 2017; Qian et al., 2021; Lu et al., 2024b). The Cretaceous cooling and exhumation event is also documented by detrital apatite fission-track data from the South Qiangtang basin (Zhang et al., 2019; Li et al., 2025) and the North Qiangtang basin (Zhang et al., 2021; Bi et al., 2023). An Eocene-Oligocene cooling

signal has also been preserved in some of these sedimentary rocks (Zhang et al., 2021; Bi et al., 2023; Li et al., 2025). However, additional AHe data are still required to constrain the most recent cooling event in thermal history modeling. Thermochronological studies on the exhumation of Eocene granitoids in the Qiangtang Plateau have so far been restricted to the Puruo Gangri granite (Zhang et al.,2021; Bi et al., 2023). Given that the thermochronological ages overlap with its crystallization age, the Eocene rapid cooling of the granite has been interpreted to be related to thermal relaxation following magmatic emplacement (Zhang et al.,2021; Bi et al., 2023).

ANALYTICAL METHODS AND THERMOCHRONOLOGY RESULTS

To more accurately constrain the temporal-spatial variation of post-Eocene uplift events and so assess the geodynamic models (Fig. 1A-G) that invoke post-Eocene exhumation, eighteen bedrock samples (15 Eocene granites and 3 volcanic rocks; Fig. S1) from the NQT were collected for zircon and apatite (U-Th)/He dating (ZHe and AHe), and apatite fission track (AFT) analysis. The Supplementary Materials provide a detailed description of the analytical methods and results. For the Eocene (> 40 Ma) and pre-Eocene uplift records, we rely on a comprehensive review of existing data (Table S9).

In general, the thermochronological ages of most Eocene granites overlap with or are close to their crystallization dates (Table S1-S4; Fig. S2-S4). Therefore, the Eocene rapid cooling (ca. 40-35 Ma; Fig. S6) derived from thermal history modeling

may record thermal relaxation related to emplacement of the granites and not erosional unroofing. This will be further assessed using geobarometric data from these intrusions. However, some Puruo Gangri and Geladandong samples have younger AFT (24.7-22.5 Ma) and AHe (28.6-12.6 Ma) ages. These rocks underwent rapid cooling and exhumation during the Oligocene and Miocene, according to thermal history models (Fig. S6). The three volcanic rocks' thermochronological ages match their eruption ages, demonstrating no major reheating since ca. 40 Ma (Table S4).

CALCULATION OF THE EXHUMATION RATE

To calculate the exhumation rate as precisely as possible, we eliminated the volcanic rocks and intrusive rocks with thermochronologic ages indistinguishable from their crystallization ages. This is because that their thermochronologic ages represent the eruptive or intrusive ages of the rocks, thus the exhumation rate calculated from these samples would be heavily overestimated. Sedimentary rocks were also not considered because they might have undergone reheating, or their ages may record the cooling of the source rocks.

Two software programs were used to calculate the exhumation rate, namely the age2exhume code (van der Beek and Schildgen, 2023) and GLIDE (Fox et al., 2014). The age2exhume code relies on a steady-state solution for the advectively perturbed geothermal gradient and employs the Dodson (1973) method to calculate closure temperatures, which inherently assumes constant topography and a steady exhumation rate during vertical exhumation (van der Beek and Schildgen, 2023). This assumption

limits the model's ability to resolve temporal variations in exhumation rates and renders it inadequate for interpreting complex thermal and exhumation histories involving processes such as burial and reheating. Furthermore, although the advective perturbation of the geotherm has a negligible effect on thermochronometric age predictions under low exhumation rates, the age2exhume code may not be appropriate for constraining the long-term evolution of mountain belts involving complex dynamic processes. This limitation arises primarily because of the model's assumptions of a constant basal temperature and fixed model thickness, which are unlikely to be valid over long geological timescales (van der Beek and Schildgen, 2023). Therefore, the exhumation rate calculated using the age2exhume code represents only the apparent, time-averaged, steady-state equivalent exhumation rate. Although the assumptions underlying the age2exhume code limit the precise quantification of exhumation rates, the general trend is likely robust, as the chosen parameters exert a consistent influence across all model predictions. Therefore, we still used the age2exhume code to rapidly calculate the apparent exhumation rate as a first-order approximation derived from the filtered thermochronology dataset.

The most effective tool currently available for calculating exhumation rates from thermochronological data is thermal-kinematic modeling using the 3-D finite-element code Pecube (Braun et al., 2012). However, significant setup requirements and relatively high computational demands restrict the spatial extent of modeled datasets to approximately 100–1000 km² (van der Beek and Schildgen, 2023), which is much smaller than that of the whole Qiangtang Plateau. As an alternative approach, we

applied the GLIDE (Fox et al., 2014) code to quantify the temporal evolution of exhumation rates. GLIDE was developed to extract exhumation histories from regional datasets through a linear inversion approach (Fox et al., 2014). The GLIDE code converts thermochronometric ages into exhumation rates based on the principle that the depth to the closure isotherm corresponds to the time integral of erosion rates from the cooling age to the present (Fox et al., 2014). Although GLIDE is well-suited for regional studies requiring a generalized model of spatial-temporal variations in exhumation rates, it is important to recognize that the temporally and spatially continuous coverage of calculated exhumation rates produced by GLIDE relies on interpolation, and the code is also not applicable in cases involving burial and reheating (Fox et al., 2014). To initialize the inverse modeling, a priori erosion rate of 0.2 ± 0.1 km/Ma, a spatial correlation length of 20 km, and a time interval of 5 Ma were assigned for a 150-million-year exhumation history. Although these parameters may have a minor impact on the accuracy of exhumation rate calculations, especially in low-resolution regions (Willett et al., 2021; Liu et al., 2023), this study emphasizes spatial and temporal variations in exhumation rates rather than absolute values. Consequently, limited effort was devoted to optimizing parameter configurations.

EMPLACEMENT DEPTH OF THE GRANITOIDS

Results of the Emplacement Depth

Given the overlap between the majority of thermochronometric ages and the crystallization ages of the Eocene granitoids, it is crucial to ascertain whether their

cooling ages were associated with thermal relaxation or exhumation. If the emplacement depths of the granitoids are shallower than the closure depths of the thermochronometric systems, the cooling ages can be attributed to thermal relaxation. Conversely, the cooling ages are related to exhumation. The crystallization pressures of hornblende, clinopyroxene, and biotite are commonly utilized to constrain the emplacement depth of the granitoids (e.g., Mutch et al., 2016). The emplacement depths of the Eocene granitoids were determined using multiple geobarometers in this study, and the detailed results are presented in Figures 3-4 and Tables S5-7.

Three samples (20QT20-3, 20QT33-4, and 20QT33-6) from the Puruogangri were collected for calculating the crystallization pressures using hornblende and biotite geobarometers. Based on the total Al content of biotite (Uchida et al., 2007), the calculated solidification pressure for the three granites ranged from 0.49 ± 0.18 kbar (1σ, same hereafter) to 0.76 ± 0.23 kbar, with an average of 0.57 ± 0.10 kbar, corresponding to an emplacement depth of 2.14 ± 0.39 km (Fig. 4). Due to most of the Fe/(Fe + Mg) ratios of hornblende lower than the recommended values of the hornblende-plagioclase geobarometer (Anderson and Smith, 1995), only the Al-in-hornblende geobarometers proposed by Schmidt (1992) and Mutch et al. (2016) were employed. After excluding the analyses that altered into actinolite, the calculated emplacement depths of the granites varied from 1.7 ± 1.6 km to 5.7 ± 1.2 km, with average emplacement depths of 2.85 ± 0.73 km and 5.30 ± 0.73 km (Fig. 4), respectively. Additionally, if the actinolite records a crystallization history under sub-solidus condition, the calculated average depth using the geobarometer of Mutch

et al. (2016) and the compositions of actinolite was about 3.04 ± 0.75 km.

Sample 21QT77-6 was collected from the Geladandong to determine the crystallization depth using hornblende and biotite geobarometers. The results show that the biotite and hornblende inclusions within the potassic-feldspar (Fig. 3C) show a significantly greater crystallization depth compared to other crystals. Based on the Al-in-biotite geobarometer (Uchida et al., 2007), the calculated emplacement depths were 2.8 ± 1.2 km and 1.6 ± 0.8 km, respectively. However, the hornblende inclusion's core indicated a crystallization depth of approximately 10-13 km (Schmidt, 1992; Mutch et al., 2016). The inconsistent results obtained from the two different geobarometers were likely due to subsequent melt-crystal interaction or thermal alteration, as evidenced by the presence of heterogeneous zoning in the hornblende inclusion that underwent metasomatism by later quartz (Fig. 3C). The estimated depth of crystallization, based on the remaining hornblende grains, ranged from 3.0 ± 1.0 km to 5.3 ± 1.0 km (Fig. 4; Schmidt, 1992; Mutch et al., 2016).

Due to the Eocene granitoids from Qoima Co, Meiriqie Co, and Maliaoshan being porphyries, the pressure estimation derived from the hornblende, biotite, and clinopyroxene phenocrysts likely reflects the crystallization conditions of a deep magma chamber rather than the emplacement depth of the host rocks. The pressures calculated from these samples, therefore, may overestimate the actual emplacement depth and should be treated with caution. The hornblende and clinopyroxene phenocrysts from the Qoima Co syenite porphyry (21QT82-1) are characterized by obvious positive zoning, with dark grey cores in the backscattered electron (BSE)

images (Fig. 3F-G). According to the Al-in-hornblende geobarometers (Schmidt, 1992; Mutch et al., 2016), the calculated crystallization depth was about 11-13 km (Fig. 4). The clinopyroxene core exhibits higher Mg# values compared to its mantle or rim, indicating a greater likelihood of equilibrium with the melts. Therefore, only the core compositions of clinopyroxene were used to estimate the crystallization conditions. The estimated depth of crystallization ranged from 6.2 ± 2.3 km to 20.2 ± 3.3 km, employing the recently developed clinopyroxene-only geobarometers (Fig. S8; Putirka, 2008; Wang et al., 2021; Higgins et al., 2022; Ágreda-López et al., 2024). Conversely, the clinopyroxene phenocrysts from the Meiriqie Co porphyry (21QT42-4, 21QT59-1) exhibit no apparent textural or composition zoning (Fig. 3D-E). The calculated crystallization depth from these grains varied from 1.59 ± 0.25 km to 14.4 ± 4.2 km (Fig. 4). Additionally, the biotite geobarometer yielded a crystallization depth of 4.7 ± 0.9 km for sample 21QT59-1 (Fig. 4). The hornblende phenocrysts from the Maliaoshan diorite porphyry display apparent textural zoning (Fig. 3H), while the calculated crystallization depth for these grains yielded a relatively clustered range at 21-27 km (Fig. 4). The biotite in the matrix, however, yielded a lower crystallization depth of 5.1 ± 0.9 km (Fig. 4).

Uncertainties and interpretations of the Geobarometers

The calculated emplacement depths for the Eocene granitoids, derived from various geobarometers, indicate that, apart from the Puruo Gangri and Geladandong granites, which have relatively consistent emplacement depths, the crystallization

287 depths of the porphyries vary significantly (Table 1). Thus, it is essential to evaluate
288 the uncertainties associated with these geobarometric estimates.

289 The Al-in-hornblende barometer is one of the most widely used methods for
290 estimating the solidus pressure of granitic intrusions (e.g., Mutch et al., 2016).
291 However, significant discrepancies or uncertainties often exist among different
292 geobarometers. For instance, although the geobarometer of Schmidt (1992) was
293 experimentally calibrated using tonalite-granodiorite compositions, it may
294 overestimate crystallization pressure by a factor of two or more under conditions of
295 high temperature and low oxygen fugacity (Anderson and Smith, 1995). The
296 experimentally recalibrated hornblende geobarometer of Mutch et al. (2016) is valid
297 down to the minimum pressures at which amphibole crystallizes (~0.5 kbar) and
298 spans a wide range of near-solidus temperatures. All the hornblendes analyzed exhibit
299 low Fe/(Fe+Mg) ratios (< 0.5; Table S5), indicative of high oxygen fugacity
300 (Anderson and Smith, 1995). Therefore, oxygen fugacity exerts minimal influence on
301 the overestimation of crystallization pressure. However, the hornblende phenocrysts
302 from Qoima Co and Maliaoshan have relatively higher crystallization temperatures
303 (~730–787 °C; Table S5) compared to those observed in near-solidus experimental
304 conditions (Anderson and Smith, 1995), as estimated using the
305 hornblende-plagioclase thermometry of Holland and Blundy (1994). Thus, the
306 hornblende barometer derived from these samples would yield erroneously elevated
307 pressure estimates.

308 Biotite is a potentially valuable mineral for estimating the solidification pressure

of granitic intrusions (Mutch et al., 2016). Uchida et al. (2007) proposed an empirical Al-in-biotite geobarometer based on the correlation between biotite's aluminum content and solidification pressure, as independently constrained by sphalerite and hornblende geobarometers. The solidification pressure estimates for the Puruo Gangri and Geladandong granites derived from the Al-in-biotite geobarometer are generally consistent with those obtained using the Al-in-hornblende geobarometer within error. Although biotite phenocrysts from the Meiriqiecuo area and biotite matrix from the Maliaoshan area suggest crystallization depths of approximately 5 km, further experimental validation is currently required to confirm the reliability of these estimates.

Although clinopyroxene barometers can be used as an alternative to estimate the solidification depth of intrusions, they generally exhibit greater uncertainty compared to hornblende barometers. For instance, the widely used clinopyroxene-only barometer of Putirka (2008), which is thermodynamically calibrated, has a standard error of 3.1 kbar. In recent years, numerous clinopyroxene-only and clinopyroxene-liquid thermobarometers have been developed using machine learning approaches (e.g., Wang et al., 2021; Higgins et al., 2022; Ágreda-López et al., 2024). Among these, the most recent model by Ágreda-López et al. (2024) appears to be the most robust, as it incorporates a bias correction procedure to address the "regression to the mean" effect and is trained on comprehensive experimental datasets of clinopyroxene–liquid equilibria (Jorgenson et al., 2022; Ágreda-López et al., 2024). Nonetheless, further high-quality experimental and natural data are still required to

refine these machine learning–based thermobarometers, particularly experimental data in which the starting materials closely match those of natural samples.

In summary, the Puruo Gangri and Geladandong granites were likely emplaced at depths of approximately 2-5 km. Such emplacement depths are generally lower than the closure depth of the ZHe isotopic system. Therefore, thermochronology dates that overlap with corresponding crystallization ages likely indicate thermal relaxation rather than exhumation signals related to erosion. However, accurately determining the emplacement depths of the porphyries from Qoima Co, Meiriqie Co, and Maliaoshan remains challenging. Based on phenocryst crystallization depths, the emplacement depths of these porphyries may range from less than 2 km to over 20 km. If these porphyries were emplaced at greater depths (e.g., >7–8 km), the Eocene rapid cooling recorded in these samples is likely associated with exhumation; otherwise, it may reflect thermal relaxation alone. However, even if the rapid cooling of these porphyries during the Eocene (ca. 40–35 Ma; Fig. S6) was driven by exhumation, the fact that their AHe ages overlap with the crystallization ages indicates that significant exhumation did not occur after the late Eocene (<35 Ma).

GEOSPATIAL ANALYSIS

Calculation of Apparent Exhumation Rate

To determine the spatial and temporal patterns of rock exhumation across the whole Qiangtang Plateau, we firstly use the *age2exhume* code (van der Beek and Schildgen, 2023) to calculate the apparent exhumation rates from multiple

353 thermochronometric systems. Although this approach is simplified due to the
354 assumption of steady, vertical rock uplift and unchanging topography when
355 calculating exhumation rates, it allows for the rapid generation of a schematic
356 representation of apparent exhumation rates from regional thermochronometric
357 datasets.

358 Our new thermochronology along with published data were used to calculate the
359 exhumation rates shown in Table S9. Based on the α-β quartz transition in the upper
360 crust of the Qiangtang terrane, the initial geothermal gradient of 39 °C/km (Zhou et
361 al., 2019) was used during the calculation. To calculate the local mean elevation, we
362 used the ESRI's ArcMap version 10.8.1 software and a standard 90 m resolution
363 Shuttle Radar Topography Mission (SRTM) digital elevation dataset (DEM)
364 (https://doi.org/10.11888/Geogra.tpdc.270486). The detailed procedures regarding
365 how to obtain the Δh value for each sample are given in the Appendix B of van der
366 Beek and Schildgen (2023). All other parameters during the calculation were set at the
367 default values of van der Beek and Schildgen (2023).

368

369 **Calculation of Slope, Relief, Precipitation, and the Distance from Faults**

370 The ArcMap software and the SRTM DEM were used to efficiently calculate the
371 slope and relief for all samples across the Qiangtang Plateau. The calculation of slope
372 can be found within the "3D Analyst Tools-Raster Surface" tool in Arc Toolbox. The
373 calculation of the relief was performed using the Focal Statistic function, which is
374 accessible via the "Spatial Analyst Tools-Neighborhood" tool within the Arc Toolbox.

Subsequently, the Raster Calculator (Spatial Analyst Tools-Map Algebra) was employed to extract the relief of the Qiangtang Plateau. When calculating the relief, a circular area with a radius of ~5 km was used. The annual precipitation data was obtained from the WorldClim version 2.1 database at a spatial resolution of 1 km (https://worldclim.org). Finally, the Extract Values to Points function (Spatial Analyst Tools-Extraction) was employed to extract the slope, relief, and precipitation data for each sample from the above calculated raster data.

The faults from Yakovlev et al. (2019) were vectorized using the ArcMap software. Subsequently, the Near tool (Analysis Tools-Proximity) within the Arc Toolbox was employed to calculate the shortest distance between the sample and either normal or reverse faults.

Relationship between Apparent Exhumation Rate and Slope, Relief, Precipitation, and the Distance from Faults

The calculated apparent exhumation rate, slope, relief, precipitation, and the distance from faults for each sample are provided in Table S9. When all samples are considered, the patterns of spatial variation in exhumation are found to be irregular, particularly for those calculated using AFT and AHe ages. However, if the unreasonable exhumation rates that derived from sedimentary, volcanic, and intrusive rocks were excluded, the apparent exhumation rates seem to migrate outward (Fig. 5). Accordingly, these unreasonable exhumation rates were excluded from subsequent discussion. Given that most Eocene granites experienced minimal exhumation since

their emplacement, we divided the thermochronology data into two groups with a boundary of approximately 40 Ma to ascertain whether disparate exhumation patterns occurred since the formation of the Proto-Tibetan Plateau.

If the exhumation was related to the activation of faults, it would be expected that rocks in closer proximity to the fault would be exhumed at a faster rate than those situated at a greater distance from the fault. Consequently, a negative correlation between the apparent exhumation rate and the distance to the fault would be identified. However, an evident correlation between the apparent exhumation rate and the distance to normal or reverse faults was not observed when all magmatic rocks were taken into account (Fig. 6A-D). Considering that the closure depth (Zc) of ZFT is ~ 6 km (assumed the geothermal gradient is 39 °C/km; Zhou et al., 2019), it can be concluded that a fault plane deeper than this depth would not disturb the thermochronometric systems. Accordingly, the horizontal distance (H) between the fault and the sample susceptible to impact from faulting is a function of the dipping angle (θ) of the fault. The function is expressed as $H = Zc/\tan(\theta)$. Thus, a dipping angle of 15° will result in a horizontal disturbing distance of approximately 20 km. Nevertheless, we arbitrarily take 50 km as a threshold for the purpose of evaluating the potential impact of faulting over greater distances. When the impacts of normal and reverse faults were considered separately, a slight negative correlation between exhumation and distance to faults within 20 km was observed (Fig. 6E-F; Fig. 7). It must be noted, however, that data for normal faults are limited, particularly for thermochronometric ages older than 40 Ma (Fig. 6A).

In our data, regardless of whether the effect of faulting was considered, no clear correlation was observed between apparent exhumation rate and slope, relief, and precipitation (Fig. 8A-F).

UPLIFT HISTORY AND MECHANISMS OF THE QIANGTANG PLATEAU

Outward Growth Surrounding a Linear Mountain Range before ~40-35 Ma

The thermal history modeling results for the Eocene granites (Fig. S6), estimates of paleoaltimetry (Xu et al., 2013), and previous thermochronological data (Wang et al., 2008a; Rohrmann et al., 2012) have clearly shown that most regions of the Qiangtang underwent negligible long-term exhumation since the emplacement of the Eocene granites. However, the details of the formation of such a proto-plateau remain incompletely understood. Therefore, we focus on the thermochronological ages older than ~40 Ma to determine how the flat plateau topography formed. After excluding the samples unsuitable for calculating exhumation rates (Fig. 5A), the resulting exhumation rate patterns exhibit orogen-orthotropic migration (Fig. 5B-D), consistent with prior studies (e.g., Bi et al., 2023). This implies that the Qiangtang underwent a gradual uplift towards the south and north. However, lateral migration of exhumation can also be observed (Fig. 5E-G), which has been overlooked in previous studies. The observed variation in apparent exhumation rate suggests that the Qiangtang initially uplifted in the central region, potentially along the central Watershed Mountains. Subsequently, the Plateau grew in both an east-west and north-south direction (Fig. 5D-G), resembling the gradual uplift surrounding an E-W-trending mountain range.

441 This scenario, which involved E-W trending growth, suggests that lateral growth has
442 occurred during the early uplift of Tibetan Plateau.
443
444 **Northeastward Expansion of the Plateau since Oligocene-Miocene**
445 The modeled spatiotemporal variation in exhumation rate using GLIDE indicates
446 that most regions of the Qiangtang Plateau did not undergo significant exhumation
447 during the Late Eocene to Early Oligocene (Fig. S10). However, localized
448 exhumation reactivated in the NQT in the Late Oligocene, particularly in the
449 Geladandong and Puruo Gangri (Fig. 9). Combining the northeastward younging
450 trend of AFT and AHe ages, crust-derived magmatism, and the identification of Early
451 Miocene high-temperature granulite xenoliths in the NQT (Fig. S8; Zhang et al.,
452 2022), we propose that the Qiangtang Plateau likely experienced northeastward
453 expansion away from the Tanggula range from the Late Oligocene to the Miocene.
454 This is also consistent with the landscape evolution of central-northern Tibet based on
455 lava field geomorphology (Law and Allen, 2020).
456 Although the modeled exhumation rates derived from compiled
457 thermochronological data suggest negligible exhumation in the SQT since the Late
458 Eocene, quantitative paleo-elevation reconstructions indicate a delayed uplift along
459 the BNS (Su et al., 2019; Fang et al., 2020; Xiong et al., 2022). The discrepancy
460 between the thermochronological results and estimates of paleoaltimetry in the central
461 valley along the BNS can primarily be attributed to the absence of Eocene or younger
462 bedrock samples, which are necessary for validating more recent exhumation events

463 in the SQT. Although a recent study has reported several Eocene (~40 Ma) dikes in
464 the Lunpola Basin, their AHe ages overlap with their emplacement ages (Lu et al.,
465 2024a). Therefore, further studies are necessary to quantify the exhumation in the
466 SQT. Collectively, we propose that the Qiangtang Plateau initially uplifted as an
467 E-W-trending range before the Eocene and subsequently expanded northeastward to
468 from a flat plateau topography during the Oligocene to Miocene (Fig. 10).
469
470 **Implications for Timing and Mechanisms of the Plateau Formation**
471 The formation of the Tibetan Plateau is the product of interaction between deep
472 lithospheric and surface processes, and many geodynamic models have been proposed
473 to interpret the formation of the plateau (Fig. 1B-H). The models that involve
474 contractional thickening include the Proto-Tibetan Plateau model (Wang et al., 2008a;
475 Rohrmann et al., 2012), the northward stepwise growth model (Tapponnier et al.,
476 2001), and the northward diffuse growth model (England and Houseman, 1986).
477 Although the Central Tibetan valley model also invokes compression to elevate the
478 Gangdese and Tanggula mountains, the uplift of the valley was attributed to
479 delamination of the Lhasa lithosphere (e.g., Ding et al., 2022). The models that
480 involve lithosphere thinning or delamination predict a rapid and overall uplift of the
481 plateau shortly after the thinning events. However, the exhumation rate mapping
482 across the Qiangtang Plateau (Figs. S12-14) does not support an instantaneous and
483 uniform uplift of the plateau even though the geophysical observations and mafic
484 magmatism (~36-29 Ma; Fig. S8) have clearly revealed that lithospheric delamination

485 occurred beneath the Plateau (inset in Fig. 2A; Li et al., 2024; Lu et al., 2025).
486 Therefore, we infer that lithospheric thinning likely occurred in localized regions,
487 such as specifically within the SQT. Nevertheless, if only thermal expansion is
488 considered, the surface uplift caused by asthenosphere upwelling due to delamination
489 is expected to be limited to less than 1 km, as indicated by isostatic calculations (Fig.
490 S12).

491 The primary trigger for compressive thickening has usually been attributed to
492 Cenozoic India-Asia collision and reactivation of pre-existing suture zones
493 (Tapponnier et al., 2001; Mulch and Chamberlain, 2006). If the uplift of the
494 Qiangtang Plateau resulted from contractional thickening, the consequent exhumation
495 would gradually migrate along with the trend of thickening, analogous to the patterns
496 of deformation and exhumation documented in the East Kunlun range, northern
497 Tibetan margin (Wang et al., 2016a, 2017). Therefore, the N-S-trending migration of
498 exhumation in Qiangtang before ~40 Ma can be reasonably attributed to
499 out-of-sequence thrusting or overthrusting along a major crustal ramp during the
500 intracontinental subduction of the Lhasa and Songpan-Ganzi lithosphere (Fig. 10A;
501 Wang et al., 2008b; Ding et al., 2022; Li et al., 2025). The weak negative correlation
502 between apparent exhumation rates and the distance from the thrust faults (Fig. 7)
503 seems to support out-of-sequence thrusting as the main trigger. Conversely, the
504 E-W-trending expansion of the plateau may result from lateral extrusion or collapse
505 resulting from N-S-trending shortening, which is also supported by the Eocene
506 N-S-trending dikes in central Qiangtang (Wang et al., 2010). It follows that the simple

northward stepwise or incremental growth models for interpreting the plateau formation cannot account for the lateral growth.

The crustal flow model predicts northeastward growth of the plateau and explains the topographic transition in northern Tibet since the Early Miocene (Wang et al., 2016b; Zhang et al., 2022), broadly matching the exhumation rate mapping in the NQT (Fig. 9A-B). The sightly earlier exhumation documented in the Geladandong and Puruogangri regions suggests that crustal weakening and melting likely commenced during the Late Oligocene in the Tanggula range, possibly facilitated by asthenospheric upwelling. Finally, it appears that climate-induced erosion processes are not the dominant mechanism in driving surface uplift, as no clear correlations have been observed between apparent exhumation rate and slope, topographic relief, and precipitation (Fig. 8).

CONCLUSIONS

Based on a systematic analysis of mineral chemistry, low-temperature thermochronology, and thermal history modeling of Eocene granitoids, combined with the spatiotemporal patterns of exhumation across the Qiangtang Plateau, this study reconstructs the uplift history and elucidates the underlying mechanisms of the plateau. The key conclusions of the study are:

(1) Most Eocene granitoids in the Qiangtang Plateau exhibit thermochronological ages that closely coincide with their crystallization ages, indicating limited post-emplacement exhumation of these intrusions since the late Eocene (<35 Ma).

(2) A two-stage growth model is proposed for the formation of the Qiangtang Plateau, involving an initial phase of outward growth from central Qiangtang as a mountain range prior to the Eocene, followed by northeastward propagation during the Oligocene to Miocene.

(3) The initial uplift of the Qiangtang Plateau was predominantly governed by N–S compressional thickening, whereas its later northeastward expansion was primarily driven by lateral crustal flow. Lithospheric thinning indirectly facilitated surface uplift by promoting crustal weakening and partial melting, while climate-induced erosional processes played a negligible role in contributing to the regional uplift.

ACKNOWLEDGMENTS

We are thankful to Science Editor Professor Mihai Ducea, Associate Editor Professor Jiyuan Yin, Professor Fei Wang, and an anonymous reviewer for their helpful comments that helped to improve our manuscript. We appreciate Xiudang Tang, Chao Guo and Yanglin Zhao for help during the analyses. Fangbin Liu, Xuemin Pan, Tiankun Xu, Zining Ma and Wenzhong Zhang are thanked for their assistance during GLIDE modeling. This study was financially supported by the National Natural Science Foundation of China (Nos. 42021002 and 42203023), the China National Science and Technology Major Project (No. 2024ZD1001103), and China Postdoctoral Science Foundation (2021M703226).

REFERNCES CITED

Ágreda-López, M., Parodi, V., Musu, A., Jorgenson, C., Carfì, A., Mastrogiovanni, F., Caricchi, L., Perugini, D., and Petrelli, M., 2024, Enhancing machine learning thermobarometry for clinopyroxene-bearing magmas: Computers & Geosciences, v. 193, p. 105707.

Anderson, J. L., and Smith, D. R., 1995, The effects of temperature and fO_2 on the Al-in-hornblende barometer: American Mineralogist, v. 80, no. 5-6, p. 549-559.

Bi, W., Li, Y., Kamp, P. J. J., Xu, G., Zhang, J., Han, Z., Du, L., Wang, C., He, H., Xu, T., and Ma, Z., 2023, Cretaceous−Cenozoic cooling history of the Qiangtang terrane and implications for Central Tibet formation: GSA Bulletin, v. 135, no. 5-6, p. 1587-1601.

Blisniuk, P. M., Hacker, B. R., Glodny, J., Ratschbacher, L., Bi, S., Wu, Z., McWilliams, M. O., and Calvert, A., 2001, Normal faulting in central Tibet since at least 13.5 Myr ago: Nature, v. 412, no. 6847, p. 628-632.

Braun, J., van der Beek, P., Valla, P., Robert, X., Herman, F., Glotzbach, C., Pedersen, V., Perry, C., Simon-Labric, T., and Prigent, C., 2012, Quantifying rates of landscape evolution and tectonic processes by thermochronology and numerical modeling of crustal heat transport using PECUBE: Tectonophysics, v. 524-525, p. 1-28.

Clark, M. K., and Royden, L. H., 2000, Topographic ooze: Building the eastern margin of Tibet by lower crustal flow: Geology, v. 28, no. 8, p. 703-706.

571 Dai, J. G., Wang, C. S., Hourigan, J., and Santosh, M., 2013, Insights into the early
572 Tibetan Plateau from (U-Th)/He thermochronology: Journal of the Geological
573 Society, v. 170, no. 6, p. 917-927.
574 Dan, W., Zhang, X.-Z., Chen, Y.-X., Tang, G.-J., Wang, Q., and Zheng, Y.-F., 2025,
575 Metamorphic evolution of Mesozoic microcontinent suture zones in the Tibet
576 region: Earth-Science Reviews, p. 105174.
577 Ding, L., Kapp, P., Cai, F., Garzione, C. N., Xiong, Z., Wang, H., and Wang, C., 2022,
578 Timing and mechanisms of Tibetan Plateau uplift: Nature Reviews Earth &
579 Environment, v. 3, p. 652-667.
580 Dodson, M. H., 1973, Closure temperature in cooling geochronological and
581 petrological systems: Contributions to Mineralogy and Petrology, v. 40, no. 3, p.
582 259-274.
583 England, P., and Searle, M., 1986, The Cretaceous-tertiary deformation of the Lhasa
584 Block and its implications for crustal thickening in Tibet: Tectonics, v. 5, no. 1, p.
585 1-14.
586 Fang, X., Dupont-Nivet, G., Wang, C., Song, C., Meng, Q., Zhang, W., Nie, J., Zhang,
587 T., Mao, Z., and Chen, Y., 2020, Revised chronology of central Tibet uplift
588 (Lunpola Basin): Science advances, v. 6, no. 50, p. eaba7298.
589 Fox, M., Herman, F., Willett, S., and May, D., 2014, A linear inversion method to
590 infer exhumation rates in space and time from thermochronometric data: Earth
591 Surface Dynamics, v. 2, no. 1, p. 47-65.

592 Higgins, O., Sheldrake, T., and Caricchi, L., 2022, Machine learning thermobarometry
593 and chemometry using amphibole and clinopyroxene: a window into the roots of
594 an arc volcano (Mount Liamuiga, Saint Kitts): Contributions to Mineralogy and
595 Petrology, v. 177, no. 1, p. 10.
596 Holland, T., and Blundy, J., 1994, Non-ideal interactions in calcic amphiboles and
597 their bearing on amphibole-plagioclase thermometry: Contributions to
598 Mineralogy and Petrology, v. 116, no. 4, p. 433-447.
599 Jorgenson, C., Higgins, O., Petrelli, M., Bégué, F., and Caricchi, L., 2022, A Machine
600 Learning-Based Approach to Clinopyroxene Thermobarometry: Model
601 Optimization and Distribution for Use in Earth Sciences: Journal of Geophysical
602 Research: Solid Earth, v. 127, no. 4, p. e2021JB022904.
603 Kapp, P., DeCelles, P. G., Gehrels, G. E., Heizler, M., and Ding, L., 2007, Geological
604 records of the Lhasa-Qiangtang and Indo-Asian collisions in the Nima area of
605 central Tibet: Geological Society of America Bulletin, v. 119, no. 7-8, p.
606 917-933.
607 Kapp, P., Yin, A., Harrison, T. M., and Ding, L., 2005, Cretaceous-Tertiary shortening,
608 basin development, and volcanism in central Tibet: GSA Bulletin, v. 117, no. 7-8,
609 p. 865-878.
610 Kapp, P., Yin, A., Manning, C. E., Murphy, M., Harrison, T. M., Spurlin, M., Lin, D.,
611 Xi-Guang, D., and Cun-Ming, W., 2000, Blueschist-bearing metamorphic core
612 complexes in the Qiangtang block reveal deep crustal structure of northern Tibet:
613 Geology, v. 28, no. 1, p. 19-22.

614 Law, R., and Allen, M. B., 2020, Diachronous Tibetan Plateau landscape evolution
615 derived from lava field geomorphology: Geology, v. 48, no. 3, p. 263-267.
616 Li, C., Zhai, Q., Dong, Y., Liu, S., Xie, C., and Wu, Y., 2009, High-pressure
617 eclogite-blueschist metamorphic belt and closure of paleo-Tethys Ocean in
618 Central Qiangtang, Qinghai-Tibet plateau: Journal of Earth Science, v. 20, no. 2,
619 p. 209-218.
620 Li, G. W., Kohn, B., Sandiford, M., Xu, Z. Q., Tian, Y. T., and Seiler, C., 2016,
621 Synorogenic morphotectonic evolution of the Gangdese batholith, South Tibet:
622 Insights from low-temperature thermochronology: Geochemistry Geophysics
623 Geosystems, v. 17, no. 1, p. 101-112.
624 Li, L., and Garzione, C. N., 2023, Upward and outward growth of north-central Tibet:
625 Mechanisms that build high-elevation, low-relief plateaus: Science Advances, v.
626 9, no. 27, p. eadh3058.
627 Li, W., He, R., Yuan, X., Schneider, F., Tilmann, F., Guo, Z., and Chen, Y. J., 2024,
628 Correlated crustal and mantle melting documents proto-Tibetan Plateau growth:
629 National Science Review, v. 11, no. 9, p. nwae257.
630 Li, Y., Bi, W., He, H., Han, Z., Wang, C., Du, L., Zhang, J., Lv, D., Wang, B., Liang,
631 Y., and Cheng, H., 2025, Cretaceous to Oligocene deformation and exhumation
632 history of the southern Qiangtang terrane and implications for the topographic
633 evolution of Central Tibet: GSA Bulletin. https://doi.org/10.1130/B37927.1

Li, Y., Wang, C., Dai, J., Xu, G., Hou, Y., and Li, X., 2015, Propagation of the deformation and growth of the Tibetan – Himalayan orogen: A review: Earth-Science Reviews, v. 143, p. 36-61.

Liu, F., Wang, M., Liu, H., and Ni, R., 2023, The Cenozoic spatiotemporal exhumation of the SE Tibetan Plateau: insight from the data mining and modeling of low-temperature thermochronology: Frontiers in Earth Science, v. 11.

Liu, J.-H., Gou, G.-N., Wang, Q., Zhang, X.-Z., and Guo, H.-F., 2022, Petrogenesis of Eocene high-silica granites in the Maliaoshan area, northern Tibet: Implications for the Eocene magmatic flare-up in the Northern Qiangtang Block: Journal of Asian Earth Sciences, v. 234, p. 105268.

Liu, M.-R., Ou, Q., Wang, Q., Qi, Y., Kerr, A. C., Wyman, D., Dan, W., Hao, L.-L., and Jiang, Z.-Q., 2024, Lithospheric Evolution and Uplift of the Tibetan Plateau During Continental Convergence: Evidence From Early Oligocene Pseudo leucite Phonolites from Southern Qian tang, Central Tibet: Journal of Petrology, v. 65, no. 11, p. egae113.

Lu, H., Li, H., Xiang, Z., Malusà, M. G., Li, C., Zhang, Z., Wu, L., Ma, X., and Pan, J., 2024a, Lithospheric strike-slip faulting in central Tibet since 35-32 Ma and implications for the incipient Asian extrusional tectonics: National Science Review, p. nwae428.

Lu, L., Jin, X., Yan, L., Li, W., Wei, T., and Shen, Y., 2024b, Early uplift and exhumation of the Tanggula granitoid pluton since the Late Cretaceous:

Implications for the stepwise topographic growth model in the eastern Qiangtang terrane: GSA Bulletin. v. 136, no. 7-8, p. 3419-3439.

Lu, Z., Gao, R., Guo, X., Li, W., Xu, X., Shi, Z., Cheng, Y., Wu, G., and Cai, Y., 2025, The funnel-shaped crustal architecture in central Tibet and its insights into the progression of lithospheric removal: Geology. v. 53, no. 7, p. 587-591.

Molnar, P., and England, P., 1990, Late Cenozoic uplift of mountain ranges and global climate change: chicken or egg?: Nature, v. 346, no. 6279, p. 29-34.

Mulch, A., and Chamberlain, C. P., 2006, The rise and growth of Tibet: Nature, v. 439, no. 7077, p. 670-671.

Mutch, E. J. F., Blundy, J. D., Tattitch, B. C., Cooper, F. J., and Brooker, R. A., 2016, An experimental study of amphibole stability in low-pressure granitic magmas and a revised Al-in-hornblende geobarometer: Contributions to Mineralogy and Petrology, v. 171, no. 10, p. 85.

Ou, Q., Wang, Q., Wyman, D. A., Zhang, C., Hao, L.-L., Dan, W., Jiang, Z.-Q., Wu, F.-Y., Yang, J.-H., Zhang, H.-X., Xia, X.-P., Ma, L., Long, X.-P., and Li, J., 2019, Postcollisional delamination and partial melting of enriched lithospheric mantle: Evidence from Oligocene (ca. 30 Ma) potassium-rich lavas in the Gemuchaka area of the central Qiangtang Block, Tibet: GSA Bulletin, v. 131, no. 7-8, p. 1385-1408.

Ou, Q., Wang, Q., Wyman, D. A., Zhang, H. X., Yang, J. H., Zeng, J. P., Hao, L. L., Chen, Y. W., Liang, H., and Qi, Y., 2017, Eocene adakitic porphyries in the central-northern Qiangtang Block, central Tibet: Partial melting of thickened

lower crust and implications for initial surface uplifting of the plateau: Journal of Geophysical Research-Solid Earth, v. 122, no. 2, p. 1025-1053.

Putirka, K. D., 2008, Thermometers and barometers for volcanic systems: Reviews in Mineralogy and Geochemistry, v. 69, no. 1, p. 61-120.

Qi, Y., Wang, Q., Wei, G.-J., Wyman, D. A., Zhang, X.-Z., Dan, W., Zhang, L., and Yang, Y.-N., 2023, Post-Collisional Silica-Undersaturated Bamaoqiongzong Volcanic Rocks from Northern Qiangtang: Indicators of the Mantle Heterogeneity and Geodynamic Evolution of Central Tibet: Journal of Petrology, v. 64, no. 1, p. egac123.

Qi, Y., Wang, Q., Wei, G.-J., Zhang, X.-Z., Dan, W., Yang, Z.-Y., Hao, L.-L., and Hu, W.-L., 2024, Oligocene High-MgO Alkali Basalts in Central Tibet: Implications for Magma–Mush Mixing and Mantle Processes: Journal of Petrology, v. 65, no. 01, p. egad091.

Qian, X., Li, Y., Dai, J., Wang, C., Han, Z., Zhang, J., and Li, H. a., 2021, Apatite and zircon (U–Th)/He thermochronological evidence for Mesozoic exhumation of the Central Tibetan Mountain Range: Geological Journal, v. 56, no. 1, p. 599-611.

Rohrmann, A., Kapp, P., Carrapa, B., Reiners, P. W., Guynn, J., Ding, L., and Heizler, M., 2012, Thermochronologic evidence for plateau formation in central Tibet by 45 Ma: Geology, v. 40, no. 2, p. 187-190.

Schmidt, M. W., 1992, Amphibole composition in tonalite as a function of pressure: an experimental calibration of the Al-in-hornblende barometer: Contributions to Mineralogy and Petrology, v. 110, no. 2-3, p. 304-310.

Staisch, L. M., Niemi, N. A., Clark, M. K., and Chang, H., 2016, Eocene to late Oligocene history of crustal shortening within the Hoh Xil Basin and implications for the uplift history of the northern Tibetan Plateau: Tectonics, v. 35, no. 4, p. 862-895.

Su, T., Farnsworth, A., Spicer, R. A., Huang, J., Wus, F. X., Liu, J., Li, S. F., Xing, Y. W., Huang, Y. J., Deng, W. Y. D., Tang, H., Xu, C. L., Zhao, F., Srivastava, G., Valdes, P. J., Deng, T., and Zhou, Z. K., 2019, No high Tibetan Plateau until the Neogene: Science Advances, v. 5, no. 3, p. eaav2189.

Tapponnier, P., Zhiqin, X., Roger, F., Meyer, B., Arnaud, N., Wittlinger, G., and Jingsui, Y., 2001, Oblique Stepwise Rise and Growth of the Tibet Plateau: Science, v. 294, no. 5547, p. 1671-1677.

Turner, S., Hawkesworth, C., Liu, J., Rogers, N., Kelley, S., and van Calsteren, P., 1993, Timing of Tibetan uplift constrained by analysis of volcanic rocks: Nature, v. 364, no. 6432, p. 50-54.

Uchida, E., Endo, S., and Makino, M., 2007, Relationship between solidification depth of granitic rocks and formation of hydrothermal ore deposits: Resource Geology, v. 57, no. 1, p. 47-56.

van der Beek, P., and Schildgen, T. F., 2023, Short communication: age2exhume – a MATLAB/Python script to calculate steady-state vertical exhumation rates from

thermochronometric ages and application to the Himalaya: Geochronology, v. 5, no. 1, p. 35-49.

van der Beek, P., Van Melle, J., Guillot, S., Pêcher, A., Reiners, P. W., Nicolescu, S., and Latif, M., 2009, Eocene Tibetan plateau remnants preserved in the northwest Himalaya: Nature Geoscience, v. 2, no. 5, p. 364-368.

Wang, C., Zhao, X., Liu, Z., Lippert, P. C., Graham, S. A., Coe, R. S., Yi, H., Zhu, L., Liu, S., and Li, Y., 2008a, Constraints on the early uplift history of the Tibetan Plateau: Proceedings of the National Academy of Sciences, v. 105, no. 13, p. 4987.

Wang, F., Feng, H., Shi, W., Zhang, W., Wu, L., Yang, L., Wang, Y., Zhang, Z., and Zhu, R., 2016a, Relief history and denudation evolution of the northern Tibet margin: Constraints from $^{40}Ar/^{39}Ar$ and (U–Th)/He dating and implications for far-field effect of rising plateau: Tectonophysics, v. 675, p. 196-208.

Wang, F., Shi, W., Zhang, W., Wu, L., Yang, L., Wang, Y., and Zhu, R., 2017, Differential growth of the northern Tibetan margin: evidence for oblique stepwise rise of the Tibetan Plateau: Scientific Reports, v. 7, no. 1, p. 41164.

Wang, Q., Hawkesworth, C. J., Wyman, D., Chung, S.-L., Wu, F.-Y., Li, X.-H., Li, Z.-X., Gou, G.-N., Zhang, X.-Z., Tang, G.-J., Dan, W., Ma, L., and Dong, Y.-H., 2016b, Pliocene-Quaternary crustal melting in central and northern Tibet and insights into crustal flow: Nature Communications, v. 7, no. 1, p. 11888.

Wang, Q., Wyman, D. A., Li, Z.-X., Sun, W., Chung, S.-L., Vasconcelos, P. M., Zhang, Q., Dong, H., Yu, Y., Pearson, N., Qiu, H., Zhu, T., and Feng, X., 2010, Eocene

742 north–south trending dikes in central Tibet: New constraints on the timing of
743 east–west extension with implications for early plateau uplift?: Earth and
744 Planetary Science Letters, v. 298, no. 1, p. 205-216.
745 Wang, Q., Wyman, D. A., Xu, J., Dong, Y., Vasconcelos, P. M., Pearson, N., Wan, Y.,
746 Dong, H., Li, C., Yu, Y., Zhu, T., Feng, X., Zhang, Q., Zi, F., and Chu, Z., 2008b,
747 Eocene melting of subducting continental crust and early uplifting of central
748 Tibet: Evidence from central-western Qiangtang high-K calc-alkaline andesites,
749 dacites and rhyolites: Earth and Planetary Science Letters, v. 272, no. 1, p.
750 158-171.
751 Wang, W., Zhang, P., Garzione, C. N., Liu, C., Zhang, Z., Pang, J., Wang, Y., Zheng,
752 D., Zheng, W., and Zhang, H., 2022, Pulsed rise and growth of the Tibetan
753 Plateau to its northern margin since ca. 30 Ma: Proceedings of the National
754 Academy of Sciences, v. 119, no. 8, p. e2120364119.
755 Wang, X., Hou, T., Wang, M., Zhang, C., Zhang, Z., Pan, R., Marxer, F., and Zhang,
756 H., 2021, A new clinopyroxene thermobarometer for mafic to intermediate
757 magmatic systems: Eur. J. Mineral., v. 33, no. 5, p. 621-637.
758 Willett, S. D., Herman, F., Fox, M., Stalder, N., Ehlers, T. A., Jiao, R., and Yang, R.,
759 2021, Bias and error in modelling thermochronometric data: resolving a potential
760 increase in Plio-Pleistocene erosion rate: Earth Surf. Dynam., v. 9, no. 5, p.
761 1153-1221.
762 Xiong, Z., Liu, X., Ding, L., Farnsworth, A., Spicer Robert, A., Xu, Q., Valdes, P., He,
763 S., Zeng, D., Wang, C., Li, Z., Guo, X., Su, T., Zhao, C., Wang, H., and Yue, Y.,

764 2022, The rise and demise of the Paleogene Central Tibetan Valley: Science
765 Advances, v. 8, no. 6, p. eabj0944.
766 Xu, C.-B., Zeng, J.-P., Wang, Q., Zhang, X.-Z., Ou, Q., Wang, J., Hao, L.-L., and
767 Chen, Y., 2022, Eocene adakitic quartz monzonites and granite porphyries from
768 the northern Qiangtang Block, central Tibet: Partial melting of sediment-rich mé
769 lange?: Frontiers in Earth Science, v. 10.
770 Xu, Q., Ding, L., Zhang, L., Cai, F., Lai, Q., Yang, D., and Liu-Zeng, J., 2013,
771 Paleogene high elevations in the Qiangtang Terrane, central Tibetan Plateau:
772 Earth and Planetary Science Letters, v. 362, p. 31-42.
773 Xu, W., Liu, L., Kohn, M. J., Liu, P., and Cai, J., 2025, Late Triassic continental
774 eclogite in the central Tibetan Plateau reveals 2500-km-long Paleo-Tethys
775 continental subduction: Geology, v. 53, no. 1, p. 23-28.
776 Xue, W., Najman, Y., Hu, X., Persano, C., Stuart, F. M., Li, W., Ma, A., and Wang, Y.,
777 2022, Late Cretaceous to late Eocene exhumation in the Nima area, central Tibet:
778 Implications for development of low relief topography of the Tibetan Plateau:
779 Tectonics, v. 41, no. 3, p. e2021TC006989.
780 Yakovlev, P. V., Saal, A., Clark, M. K., Hong, C., Niemi, N. A., and Mallick, S., 2019,
781 The geochemistry of Tibetan lavas: Spatial and temporal relationships, tectonic
782 links and geodynamic implications: Earth and Planetary Science Letters, v. 520,
783 p. 115-126.
784 Yin, J., Wang, Y., Hodges, K. V., Xiao, W., Thomson, S. N., Chen, W., Yuan, C., Sun,
785 M., Cai, K., and Sun, J., 2023, Episodic long-term exhumation of the Tianshan

786 orogenic belt: New insights from multiple low-temperature thermochronometers:
787 Tectonics, v. 42, no. 4, p. e2022TC007469.
788 Zhang, J., Li, Y., Xu, M., Dai, J., Qian, X., Han, Z., Zhang, H., and Pang, J., 2021,
789 New apatite fission track evidence from the northern Qiangtang terrane reveal
790 two-phase evolution of central Tibet: Terra Nova, v. 33, no. 1, p. 95-108.
791 Zhang, J., Sinclair, H. D., Li, Y., Wang, C., Persano, C., Qian, X., Han, Z., Yao, X.,
792 and Duan, Y., 2019, Subsidence and exhumation of the Mesozoic Qiangtang
793 Basin: Implications for the growth of the Tibetan plateau: Basin Research, v. 31,
794 no. 4, p. 754-781.
795 Zhang, X.-Z., Wang, Q., Wyman, D., Ou, Q., Qi, Y., Gou, G.-N., Dan, W., and Yang,
796 Y.-N., 2022, Tibetan Plateau growth linked to crustal thermal transitions since
797 the Miocene: Geology, v. 50, no. 5, p. 610-614.
798 Zhao, Z., Lu, H., Wang, S., Li, H., Li, C., Liu, D., Pan, J., Zheng, Y., and Bai, M.,
799 2022, The Cenozoic Multiple-Stage Uplift of the Qiangtang Terrane, Tibetan
800 Plateau: Frontiers in Earth Science, v. 10.
801 Zhao, Z. B., Bons, P. D., Stubner, K., Wang, G. H., and Ehlers, T. A., 2017, Early
802 Cretaceous exhumation of the Qiangtang Terrane during collision with the Lhasa
803 Terrane, Central Tibet: Terra Nova, v. 29, no. 6, p. 382-391.
804 Zhou, B., Liang, X., Lin, G., Tian, X., Zhu, G., Mechie, J., and Teng, J., 2019, Upper
805 Crustal Weak Zone in Central Tibet: An Implication from three-dimensional
806 seismic velocity and attenuation tomography results: Journal of Geophysical
807 Research: Solid Earth, v. 124, no. 5, p. 4654-4672.

808

809 **Figure captions**

810 **Figure 1.** Geodynamic models and paleo-elevation reconstruction of the Tibet Plateau.
811 (**A**) Proto-Tibetan Plateau model (Wang et al., 2008; Rohrmann et al., 2012), which
812 predicts negligible exhumation since the Eocene in central Tibet. (**B**) Northward
813 stepwise growth model (Tapponnier et al., 2001). The exhumation primarily occurred
814 along the suture and migrated northward in this model. (**C**) Central Tibetan valley
815 model (Ding et al., 2022) predicts exhumation occurring on both sides of the valley
816 and towards to the middle. (**D**) Northward diffuse growth model (England and
817 Houseman, 1986) predicts a gradual northward migration of exhumation and
818 N-S-trending shortening. (**E**) Lithosphere thinning model (Turner et al., 1993)
819 predicts an instantaneous and uniform exhumation. (**F**) Lower crustal flow model
820 (Clark and Royden, 2000) predicts a northeastward migration of exhumation without
821 shortening. (**G**) Climate-related model (Molnar and England, 1990). Exhumation
822 would be related to climate-related proxies in this model. (**H**) Cenozoic uplift history
823 of the Tibetan Plateau and adjacent areas based on paleo-altimetric studies (Ding et al.,
824 2022; Li and Garzione, 2023).

825

826 **Figure 2**. Tibetan Plateau topography, tectonics, and plateau formation mechanisms.
827 (**A**) Topography and tectonics of the Tibetan Plateau, with Cenozoic magmatic rocks,
828 and locations of previous paleo-altimetric studies (Ding et al., 2022). The inset shows
829 the S-wave velocity profile across the Tibetan Plateau (after Li et al., 2024). (**B-E**)

Schematic models illustrating the possible driving mechanisms responsible for the uplift of the Tibetan Plateau.

IYS—Indus-Yarlung suture; BNS—Bangong-Nujiang suture; JS—Jinsha suture; KS—Kunlun suture.

Figure 3. Backscattered electron (BSE) images of the hornblende, clinopyroxene, and biotite from the Eocene granitoids in the Tibetan Plateau.

Hb-hornblende; Cpx-clinopyroxene; Bt-biotite; Q-quartz; Pl-plagioclase; Kfs-potassic-feldspar; Ap-apatite

Figure 4. The calculated emplacement depth of the Eocene granitoids.

Hb1992-hornblende geobarometer of Schmidt (1992); Hb2016-hornblende geobarometer of Mutch et al. (2016); Bt2007-biotite geobarometer of Uchida et al. (2007); Cpx2008-clinopyroxene-only geobarometer of Putirka (2008); Cpx2021-clinopyroxene geobarometer of Wang et al. (2021); Cpx2022-clinopyroxene geobarometer of Higgins et al. (2022); Cpx2024-clinopyroxene geobarometer of Ágreda-López et al. (2024).

Figure 5. Spatial variations in apparent exhumation rate across the Qiangtang Plateau. The new and compiled data are provided in Table S9. Low-temperature thermochronological ages that represent magmatic-hydrothermal cooling, source rock cooling and reheating were not plotted. (**A**) Distribution of bedrock low-temperature

852 thermochronological samples, with superimposed major faults and their timing of
853 activity (adapted from Yakovlev et al., 2019). (**B-D**) Cross sections along 84°E, 88°E,
854 and 92°E reveal a north-south trending increase in exhumation rate away from the
855 Tanggula range, consistent with previous studies (e.g., Bi et al., 2023; Li et al., 2025).
856 (**E**) E-W-trending variation of thermochronological ages. (**F**) Contour map of the
857 apparent exhumation rate calculated using ZHe ages older than 40 Ma. (**G**) Contour
858 map of the apparent exhumation rate calculated using AHe ages older than 40 Ma.
859 The orogen-parallel variation in exhumation suggests that lateral growth of the
860 Qiangtang Plateau during its early uplift. The apparent exhumation rate is calculated
861 using the age2exhume code and is expressed as a time-averaged, steady-state
862 equivalent exhumation rate (van der Beek and Schildgen, 2023).
863 ZFT—zircon fission track; ZHe—zircon (U-Th)/He; AFT—apatite fission track; AHe
864 —apatite (U-Th)/He.
865
866 **Figure 6**. Plots of apparent exhumation rate against distance to normal and reverse
867 faults. (**A–B**) All magmatic rocks with thermochronometric ages indicative of
868 exhumation are included. (**C–D**) Only samples with thermochronometric ages
869 younger than 40 Ma are shown. (**E**) Samples located more than 50 km away from
870 reverse faults but near normal faults are plotted. (**F**) Samples situated more than 50
871 km from reverse faults and near reverse faults are displayed.
872
873 **Figure 7**. Plots of apparent exhumation rate versus the distance to the normal fault (**A**)

874 and reverse fault (**B**) for samples with thermochronometric ages older than 40 Ma.

875

876 **Figure 8**. Plots of apparent exhumation rate versus the slope, relief, and precipitation.
877 All magmatic rocks with their thermochronometric ages related to exhumation were
878 plotted in panels **A**, **C** and **E**. Conversely, samples away from both the normal and
879 reverse faults (> 50 km) were plotted in panels **B**, **D** and **F**.

880

881 **Figure 9**. The exhumation rate maps of the Qiangtang Plateau for the periods 30-25
882 Ma (**A**) and 25-20 Ma (**B**). Thermal history inverse modeling of Eocene granites from
883 the Puruo Gangri and Geladandong regions (**C-D**) reveals rapid cooling during the
884 Late Oligocene to Miocene period. The exhumation rate is calculated using the
885 GLIDE code developed by Fox et al. (2014). The Miocene granulite xenoliths from
886 the NQT in panel A were identified by Zhang et al. (2022).

887

888 **Figure 10**. Schematic model showing the growth history of the Qiangtang Plateau. (**A**)
889 Outward growth around an E-W-trending range before the Eocene. The schematic
890 inset illustrates the growth trend from T1 to T4. (**B**) Lithospheric delamination is
891 inferred to have occurred during the Early Oligocene, with surface exhumation likely
892 being restricted to a limited extent. (**C**) The northeastward expansion of the plateau
893 during the Late Oligocene to Miocene is due to crustal melting and flow.

894

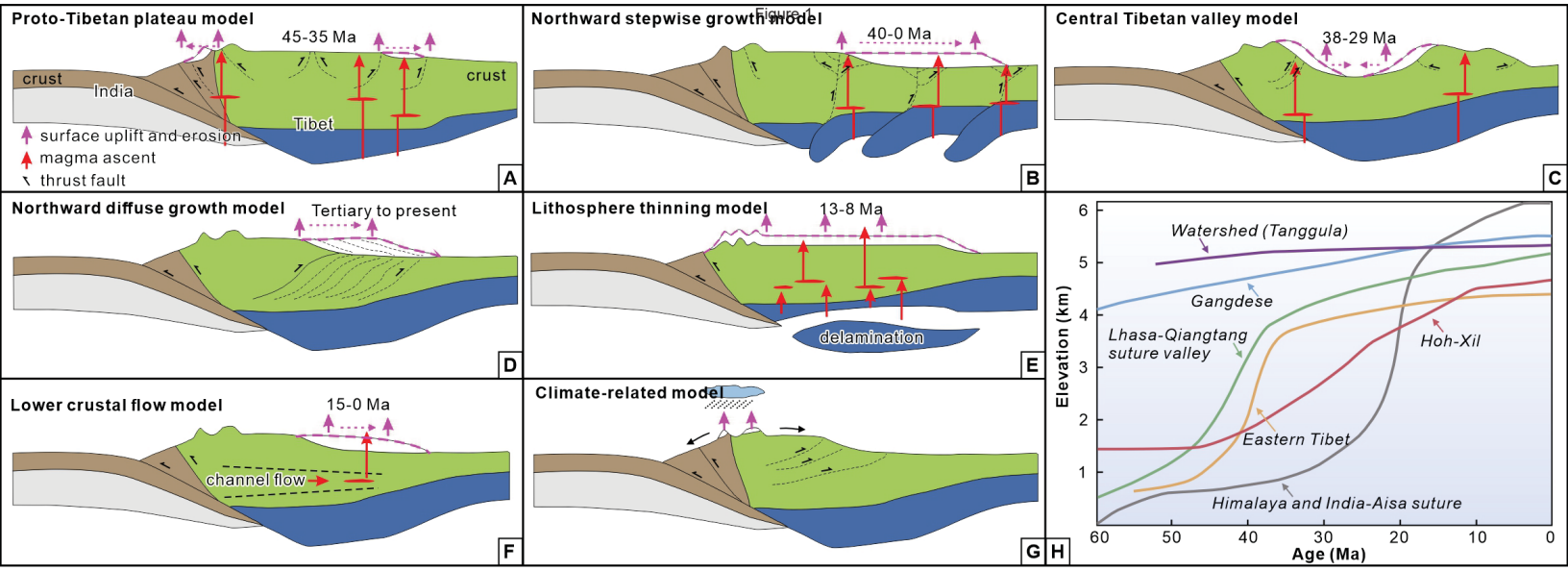
Proto-Tibetan plateau model
45-35 Ma
crust
India
Tibet
crust
surface uplift and erosion
magma ascent
thrust fault
A
Northward stepwise growth model
40-0 Ma
B
Central Tibetan valley model
38-29 Ma
C
Northward diffuse growth model
Tertiary to present
D
Lithosphere thinning model
13-8 Ma
delamination
E
Lower crustal flow model
15-0 Ma
channel flow
F
Climate-related model
G
Watershed (Tanggula)
Gangdese
Lhasa-Qiangtang suture valley
Hoh-Xil
Eastern Tibet
Himalaya and India-Aisa suture
Elevation (km)
Age (Ma)
H

Figure 1

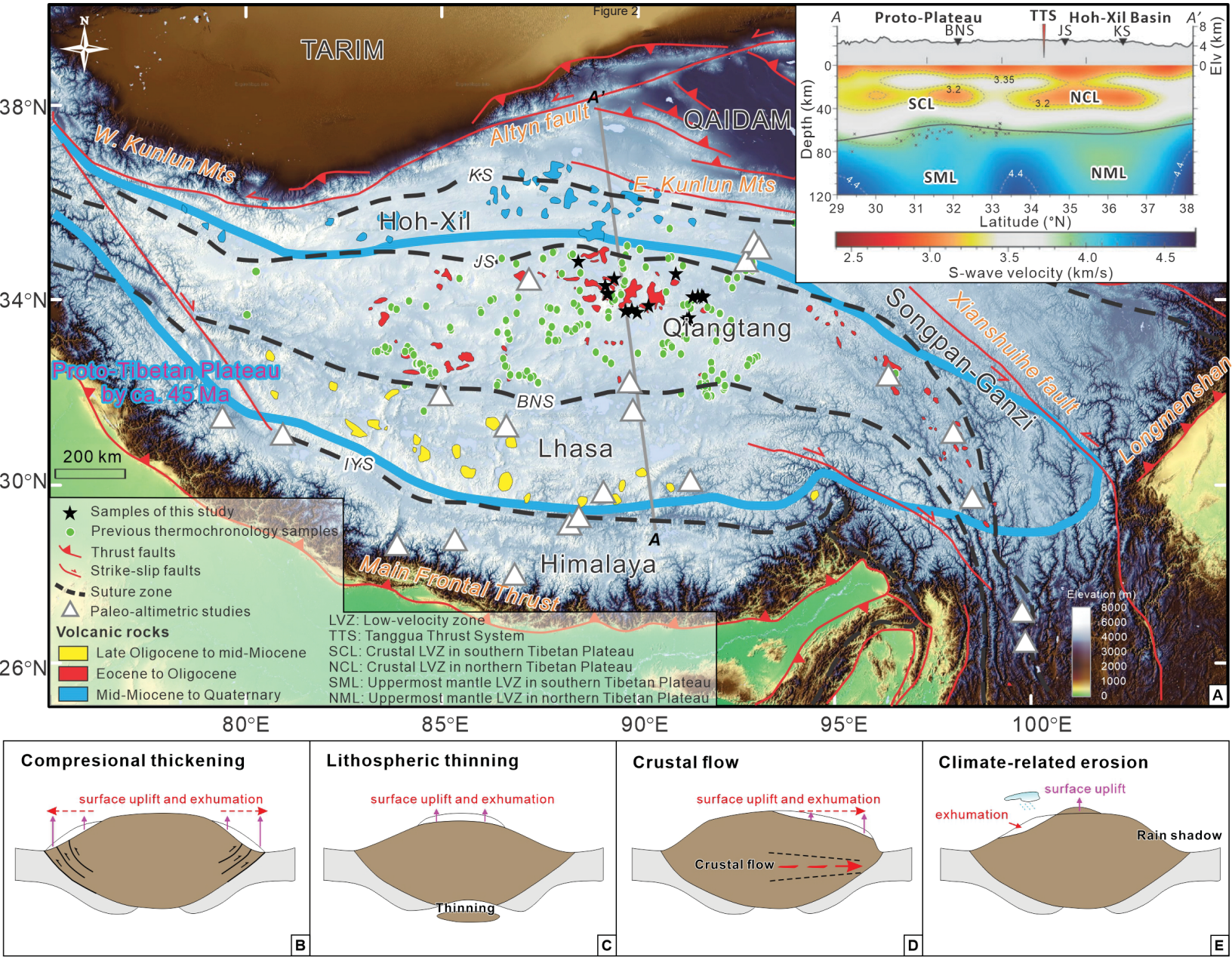
Figure 2
TARIM
QAIDAM
Hoh-Xil
Qiangtang
Lhasa
Himalaya
W. Kunlun Mts
E. Kunlun Mts
Altyn fault
KS
JS
BNS
IYS
Songpan-Ganzi
Xianshuihe fault
Longmenshan
Main Frontal Thrust
Proto-Tibetan Plateau by ca. 45 Ma
200 km
A
A'
38°N
34°N
30°N
26°N
80°E
85°E
90°E
95°E
100°E
Samples of this study
Previous thermochronology samples
Thrust faults
Strike-slip faults
Suture zone
Paleo-altimetric studies
Volcanic rocks
Late Oligocene to mid-Miocene
Eocene to Oligocene
Mid-Miocene to Quaternary
LVZ: Low-velocity zone
TTS: Tanggua Thrust System
SCL: Crustal LVZ in southern Tibetan Plateau
NCL: Crustal LVZ in northern Tibetan Plateau
SML: Uppermost mantle LVZ in southern Tibetan Plateau
NML: Uppermost mantle LVZ in northern Tibetan Plateau
Elevation (m)
8000
6000
4000
3000
2000
1000
0
Proto-Plateau
TTS
Hoh-Xil Basin
BNS
JS
KS
Elv (km)
Depth (km)
SCL
NCL
SML
NML
3.2
3.35
4.4
Latitude (°N)
S-wave velocity (km/s)
2.5
3.0
3.5
4.0
4.5

Compresional thickening
surface uplift and exhumation
B
Lithospheric thinning
surface uplift and exhumation
Thinning
C
Crustal flow
surface uplift and exhumation
Crustal flow
D
Climate-related erosion
surface uplift
exhumation
Rain shadow
E


Puruo Gangri
Ap
Bt
Hb
Bt
20QT20-3
BED-C 15.0kV WD 11.1mm x170 Std.P.C.62 STD 50µm
000 FOV:753x565µm 08/11/2024
A

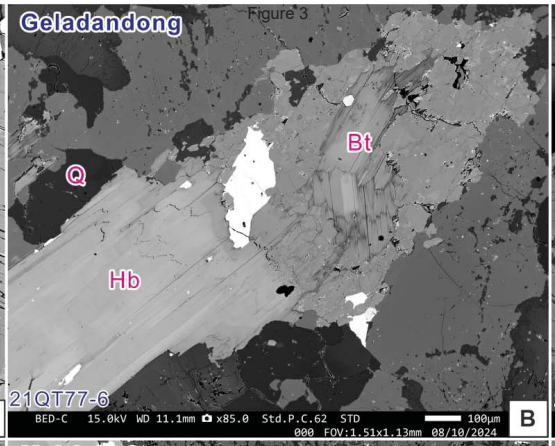
Geladandong
Bt
Q
Hb
21QT77-6
BED-C 15.0kV WD 11.1mm x85.0 Std.P.C.62 STD 100µm
000 FOV:1.51x1.13mm 08/10/2024
B

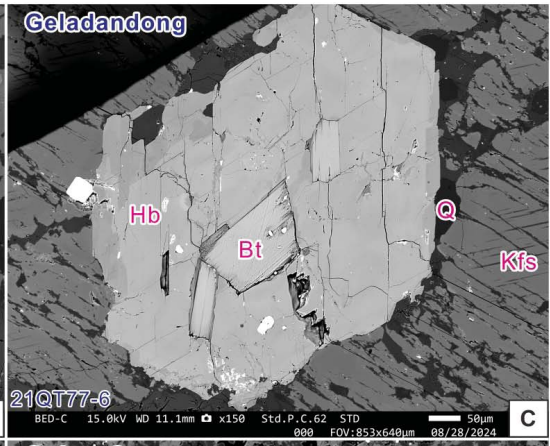
Geladandong
Hb
Q
Bt
Kfs
21QT77-6
BED-C 15.0kV WD 11.1mm x150 Std.P.C.62 STD 50µm
000 FOV:853x640µm 08/28/2024
C


Meiriqie Co
Cpx
21QT42-4
BED-C 15.0kV WD 11.1mm x130 Std.P.C.62 STD 100µm
000 FOV:985x738µm 08/11/2024
D

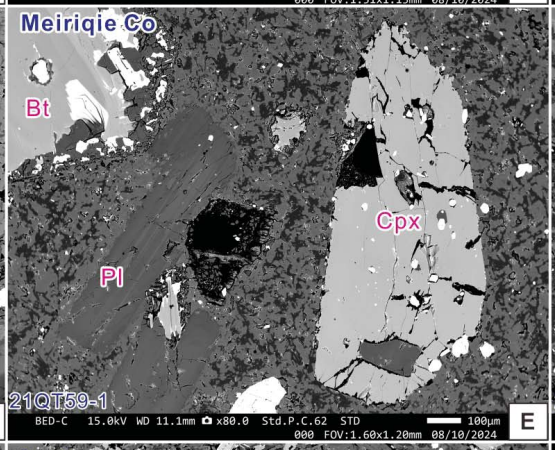
Meiriqie Co
Bt
Cpx
Pl
21QT59-1
BED-C 15.0kV WD 11.1mm x80.0 Std.P.C.62 STD 100µm
000 FOV:1.60x1.20mm 08/10/2024
E

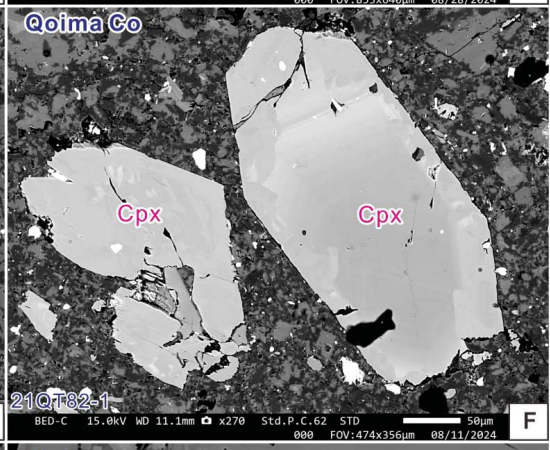
Qoima Co
Cpx
Cpx
21QT82-1
BED-C 15.0kV WD 11.1mm x270 Std.P.C.62 STD 50µm
000 FOV:474x356µm 08/11/2024
F

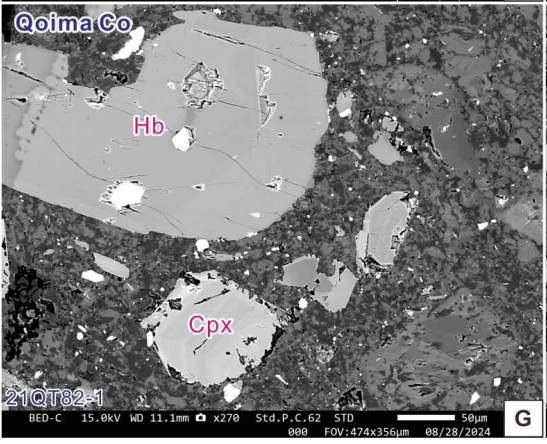
Qoima Co
Hb
Cpx
21QT82-1
BED-C 15.0kV WD 11.1mm x270 Std.P.C.62 STD 50µm
000 FOV:474x356µm 08/28/2024
G

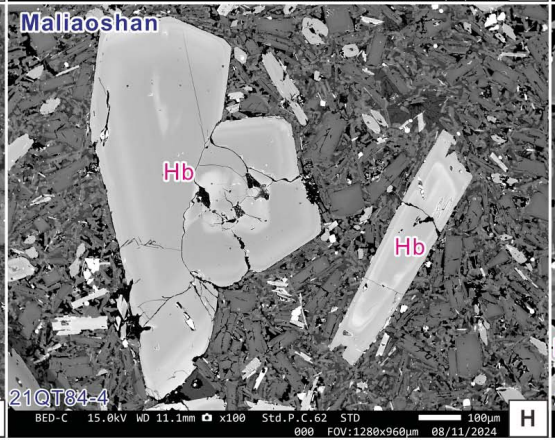
Maliaoshan
Hb
Hb
21QT84-4
BED-C 15.0kV WD 11.1mm x100 Std.P.C.62 STD 100µm
000 FOV:1280x960µm 08/11/2024
H


Maliaoshan
Pl
Bt
Q
Hb
21QT84-4
BED-C 15.0kV WD 11.1mm x550 Std.P.C.62 STD 10µm
000 FOV:233x175µm 08/28/2024
I

Figure 4

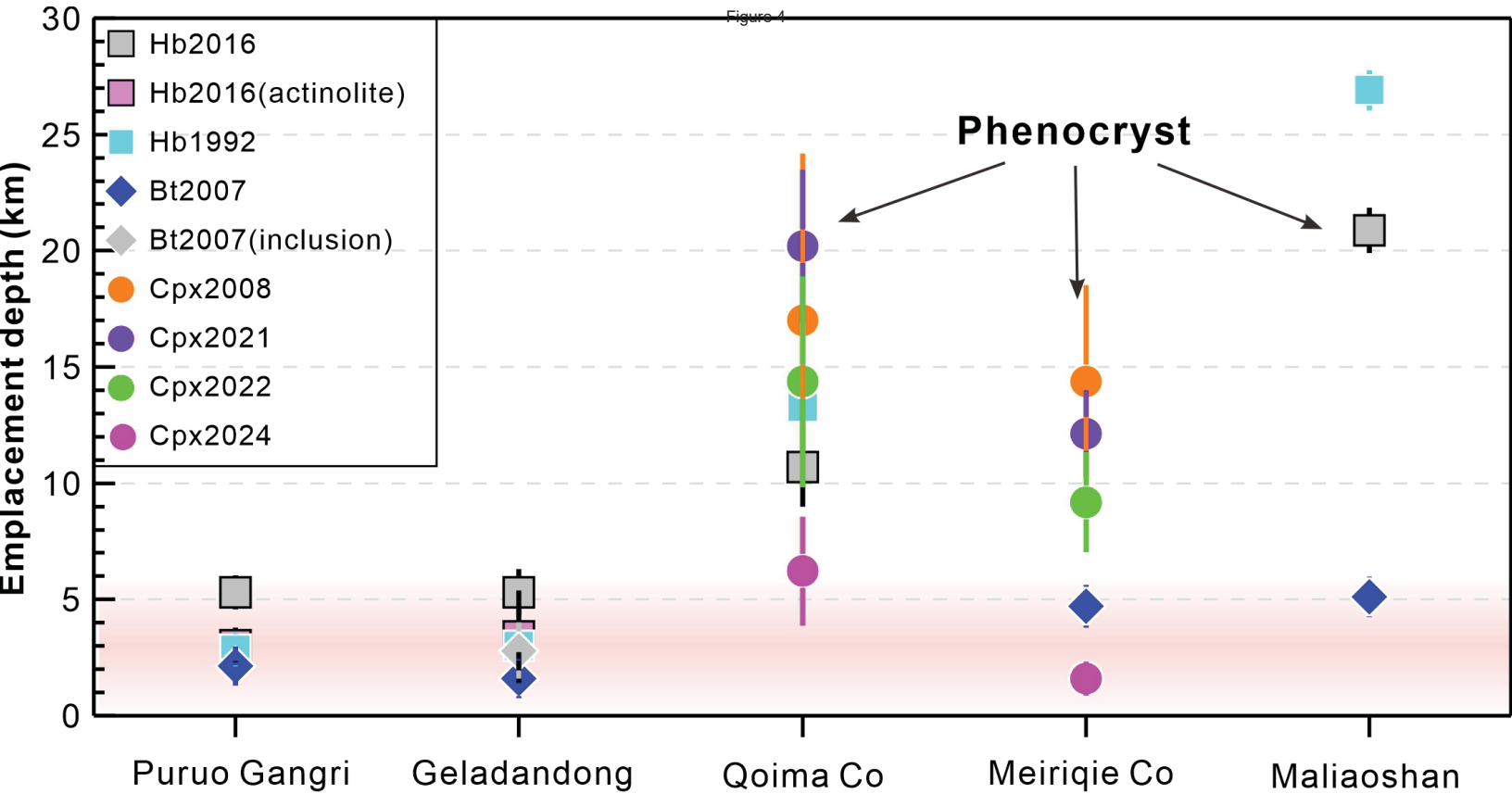
Hb2016
Hb2016(actinolite)
Hb1992
Bt2007
Bt2007(inclusion)
Cpx2008
Cpx2021
Cpx2022
Cpx2024
Phenocryst
Emplacement depth (km)
30
25
20
15
10
5
0
Puruo Gangri
Geladandong
Qoima Co
Meiriqie Co
Maliaoshan

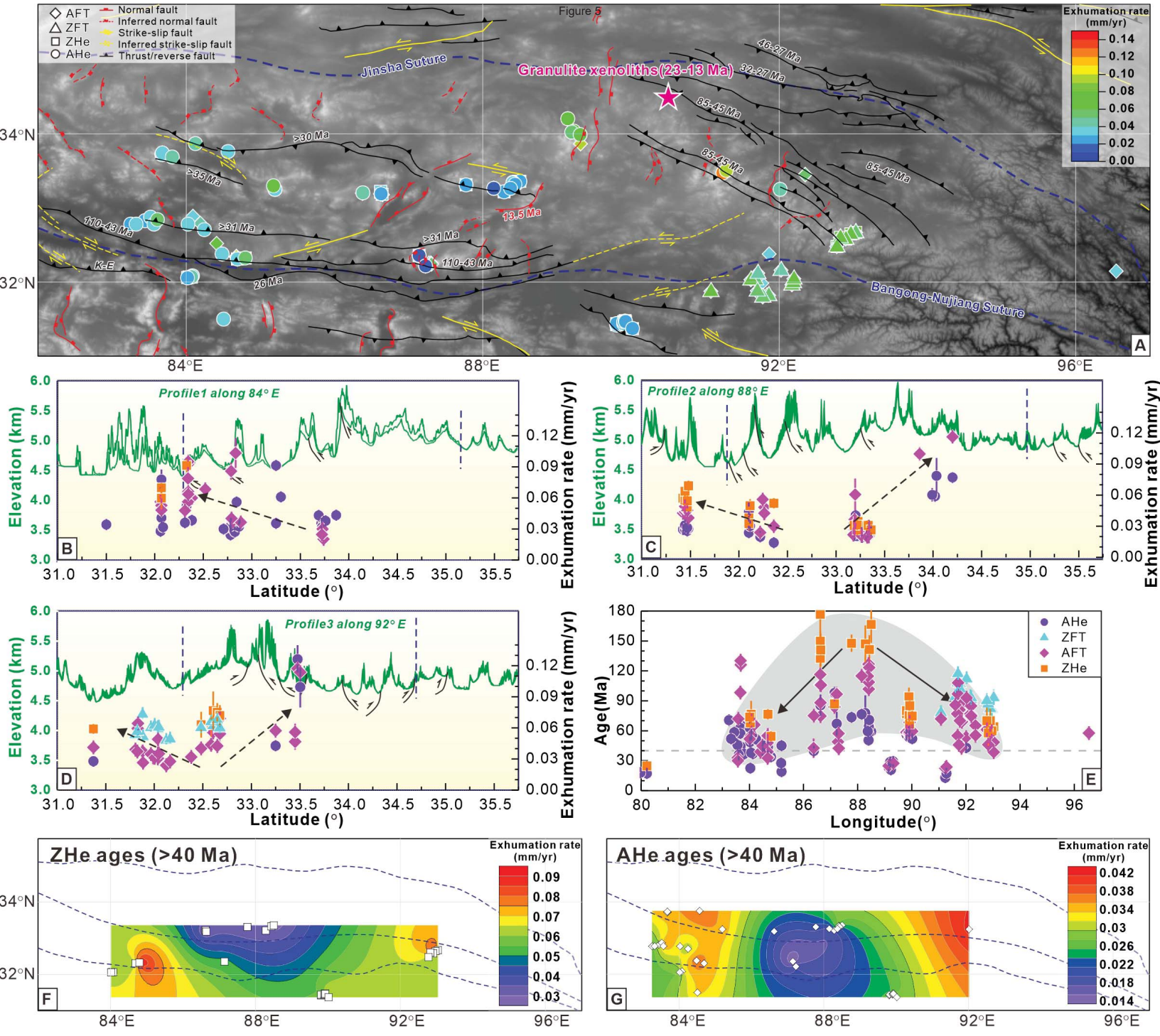
AFT
ZFT
ZHe
AHe
Normal fault
Inferred normal fault
Strike-slip fault
Inferred strike-slip fault
Thrust/reverse fault
Figure 5
Exhumation rate (mm/yr)
0.14
0.12
0.10
0.08
0.06
0.04
0.02
0.00
Jinsha Suture
Granulite xenoliths(23-13 Ma)
46-27 Ma
32-27 Ma
85-45 Ma
85-45 Ma
85-45 Ma
>30 Ma
>35 Ma
13.5 Ma
110-43 Ma
>31 Ma
>31 Ma
110-43 Ma
K-E
26 Ma
Bangong-Nujiang Suture
34°N
32°N
84°E
88°E
92°E
96°E
A
Profile1 along 84° E
Elevation (km)
Exhumation rate (mm/yr)
Latitude (°)
B
Profile2 along 88° E
C
Profile3 along 92° E
D
Age(Ma)
Longitude(°)
AHe
ZFT
AFT
ZHe
E
ZHe ages (>40 Ma)
F
AHe ages (>40 Ma)
G

Figure 6

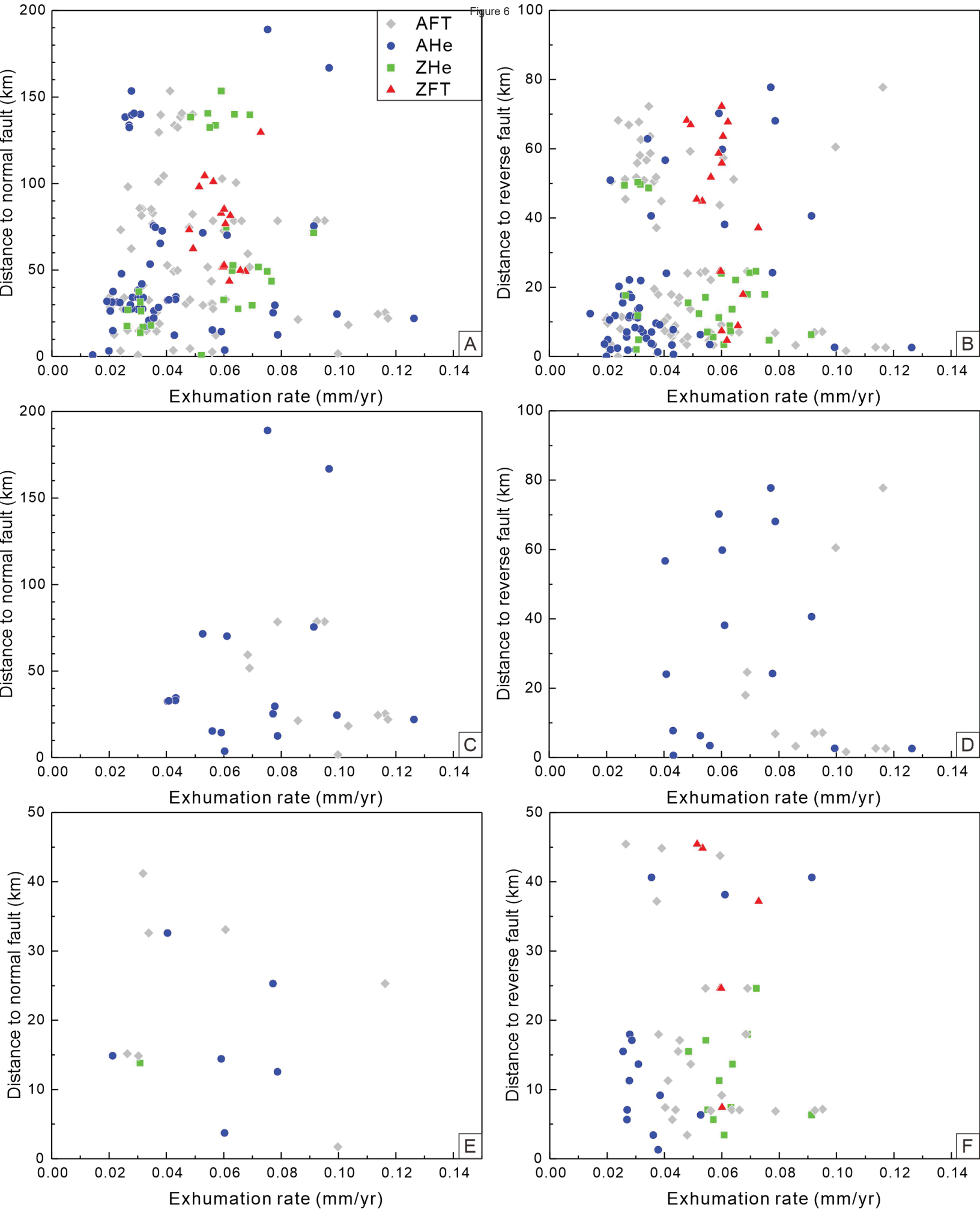
AFT
AHe
ZHe
ZFT
Distance to normal fault (km)
Distance to reverse fault (km)
Exhumation rate (mm/yr)
A
B
C
D
E
F

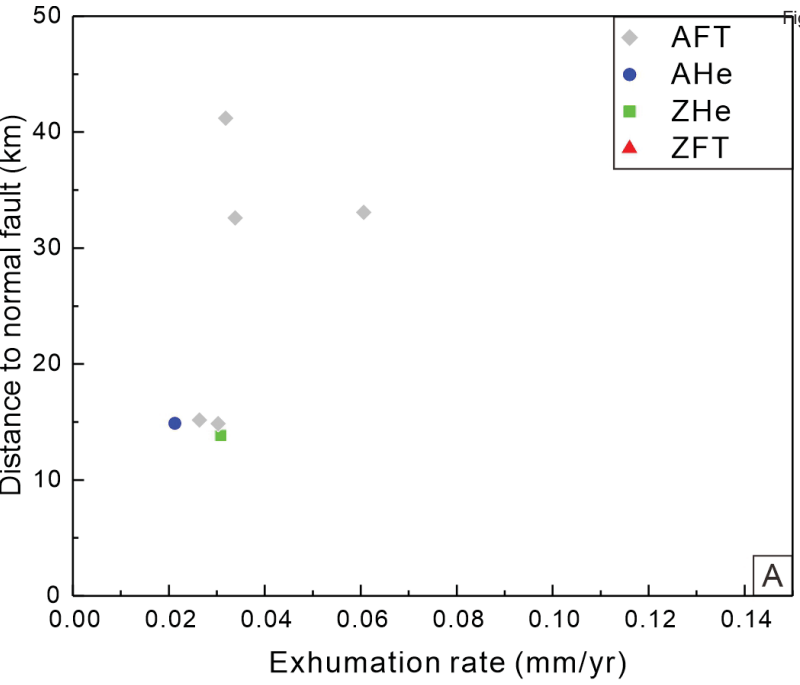
AFT
AHe
ZHe
ZFT
Distance to normal fault (km)
Exhumation rate (mm/yr)
A
0
10
20
30
40
50
0.00
0.02
0.04
0.06
0.08
0.10
0.12
0.14

Figure 7

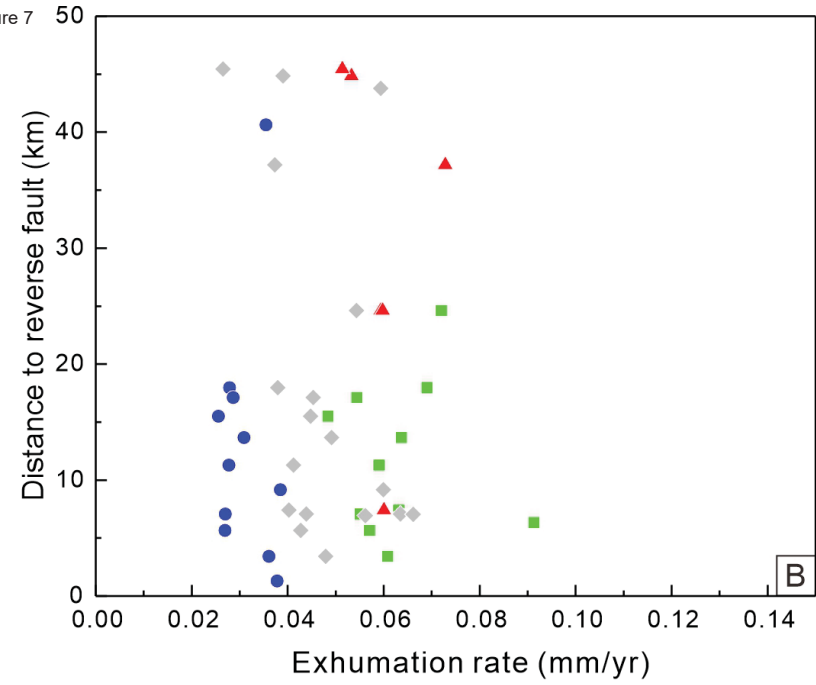
Distance to reverse fault (km)
Exhumation rate (mm/yr)
B
0
10
20
30
40
50
0.00
0.02
0.04
0.06
0.08
0.10
0.12
0.14

Figure 8

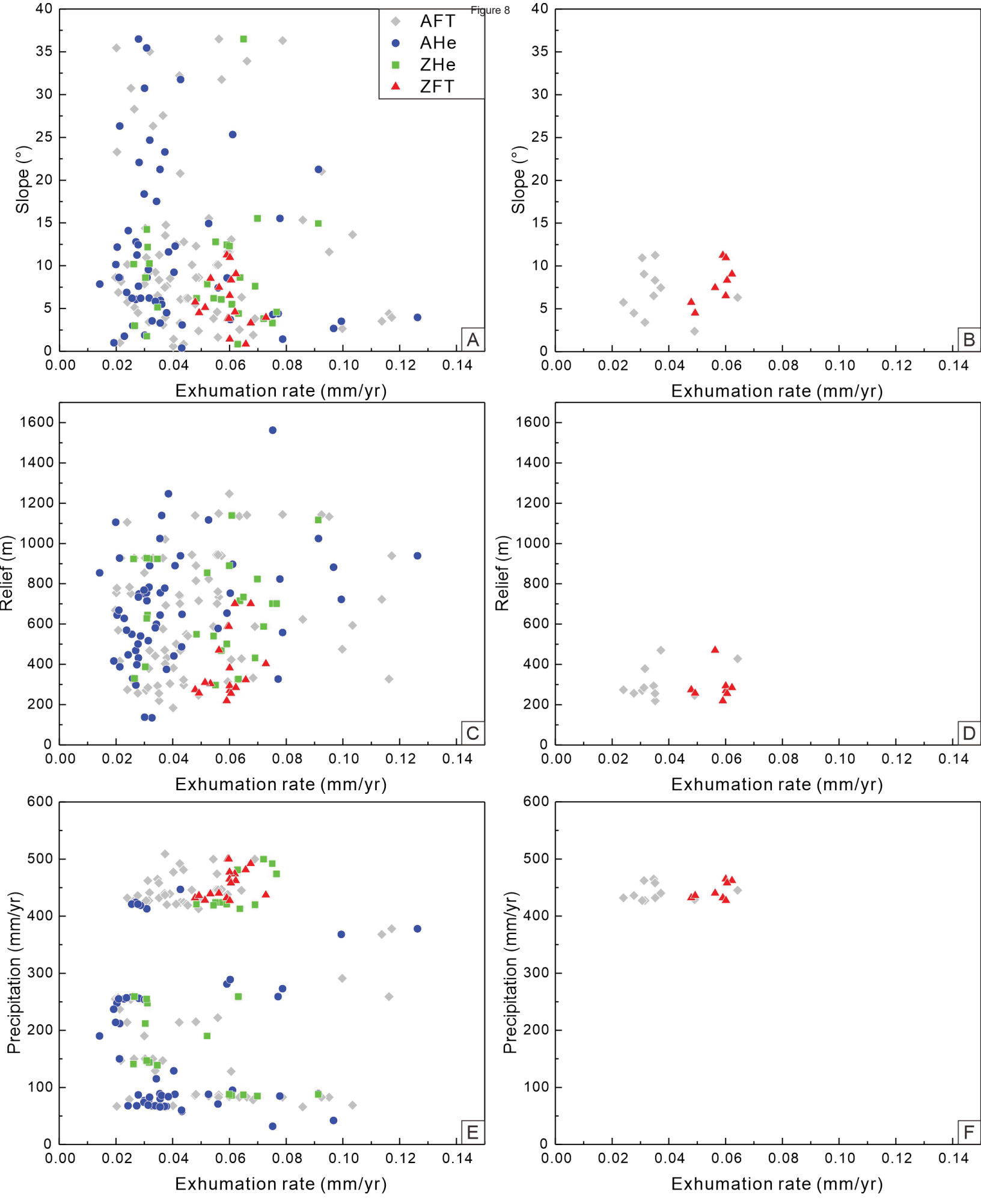
AFT
AHe
ZHe
ZFT
Slope (°)
Relief (m)
Precipitation (mm/yr)
Exhumation rate (mm/yr)
A
B
C
D
E
F

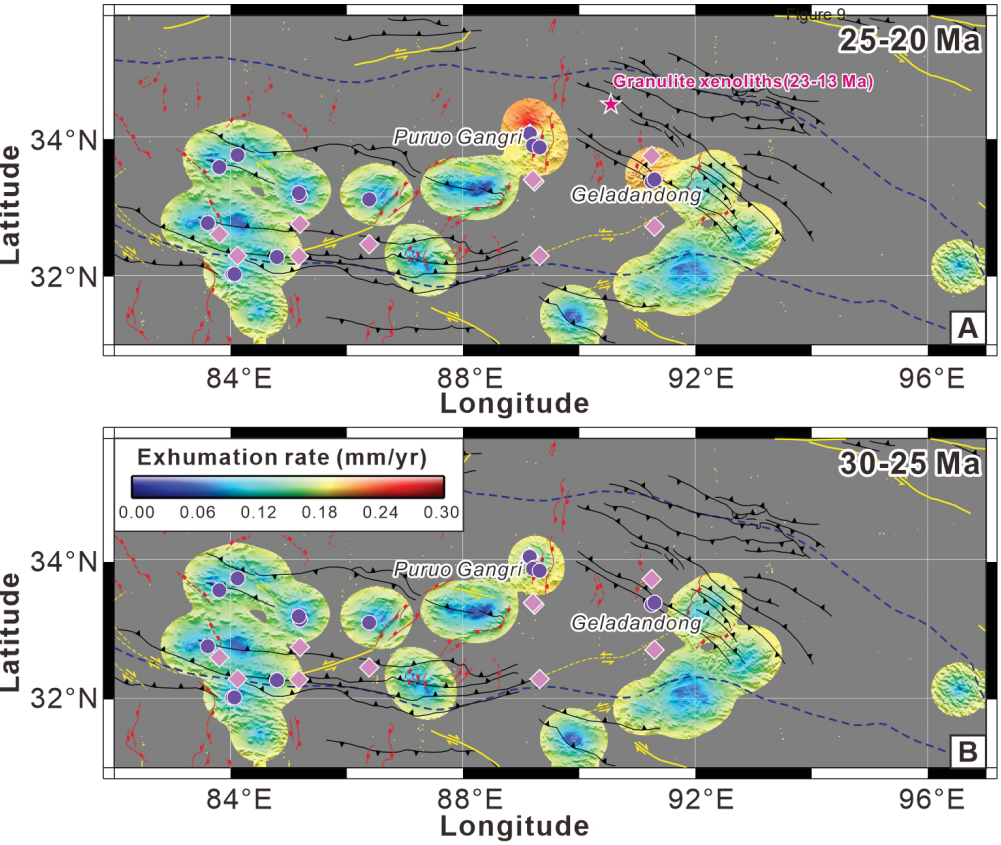
Figure 9
25-20 Ma
Granulite xenoliths(23-13 Ma)
Puruo Gangri
Geladandong
34°N
32°N
Latitude
84°E
88°E
92°E
96°E
Longitude
A
Exhumation rate (mm/yr)
0.00 0.06 0.12 0.18 0.24 0.30
30-25 Ma
Puruo Gangri
Geladandong
34°N
32°N
Latitude
84°E
88°E
92°E
96°E
Longitude
B

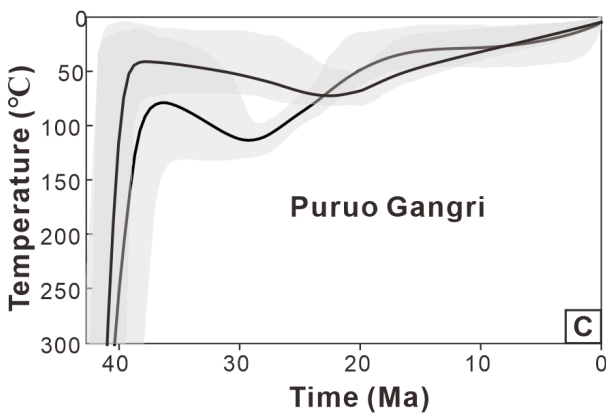
Temperature (°C)
0
50
100
150
200
250
300
40
30
20
10
0
Time (Ma)
Puruo Gangri
C

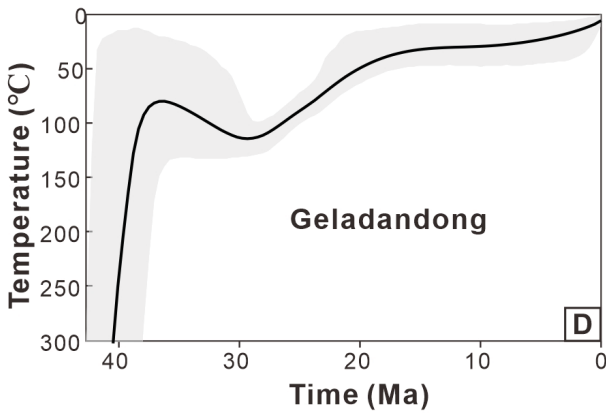
Temperature (°C)
0
50
100
150
200
250
300
40
30
20
10
0
Time (Ma)
Geladandong
D

Figure 10

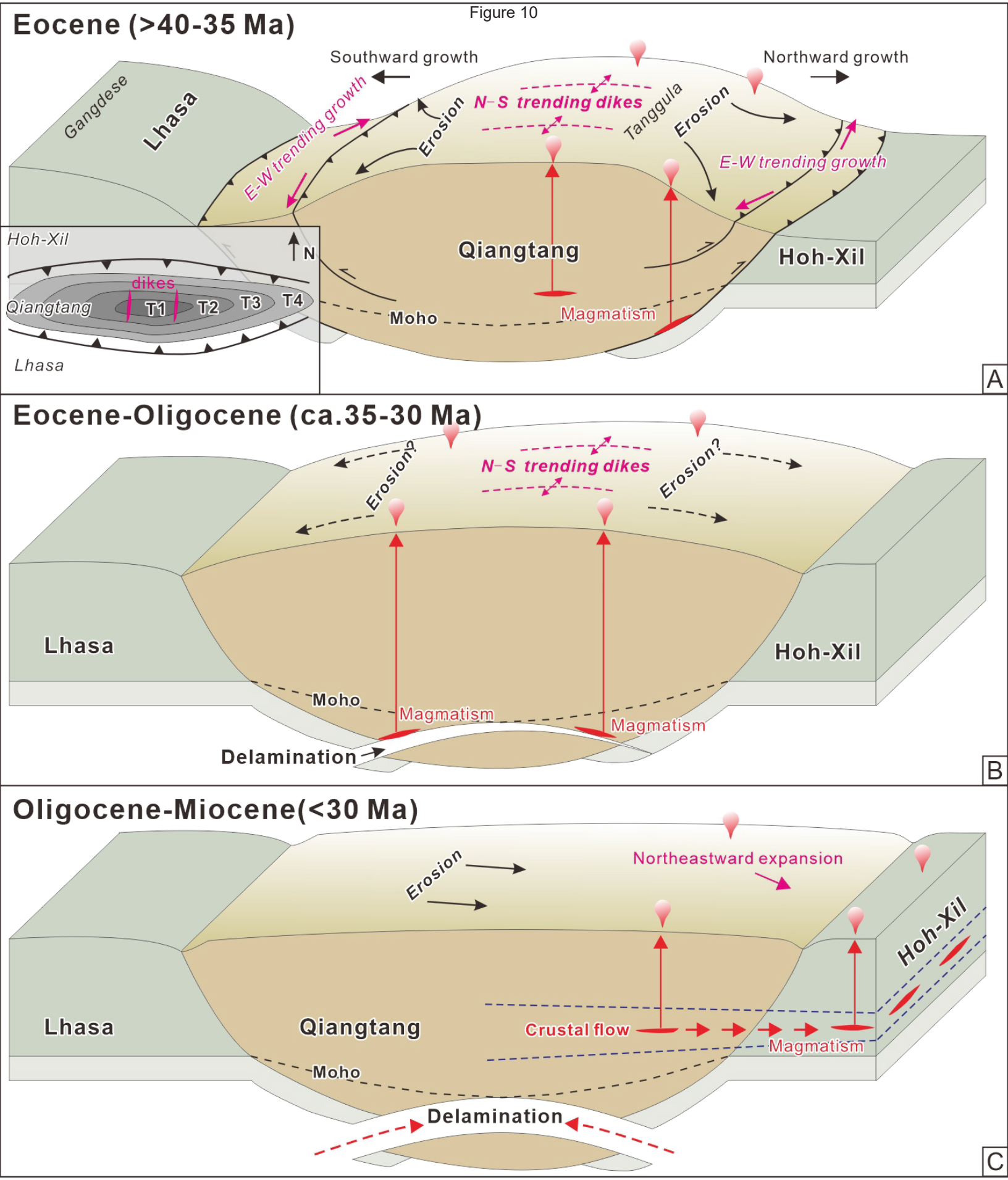
Eocene (>40-35 Ma)
Southward growth
Northward growth
Gangdese
Lhasa
E-W trending growth
Erosion
N–S trending dikes
Tanggula
Erosion
E-W trending growth
Hoh-Xil
N
dikes
Qiangtang
T1
T2
T3
T4
Lhasa
Qiangtang
Hoh-Xil
Moho
Magmatism
A
Eocene-Oligocene (ca.35-30 Ma)
Erosion?
N–S trending dikes
Erosion?
Lhasa
Hoh-Xil
Moho
Magmatism
Magmatism
Delamination
B
Oligocene-Miocene(<30 Ma)
Erosion
Northeastward expansion
Hoh-Xil
Lhasa
Qiangtang
Crustal flow
Magmatism
Moho
Delamination
C

Table 1. A summary of emplacement depth estimates for Eocene granitoids across the Qiangtang Plateau using different geobarometers

Sample No.	Locality	Lithology	Hb1992 (km)	Hb2016† (km)	Bt2007‡ (km)	Cpx2008 (km)	Cpx2021 (km)	Cpx2022 (km)	Cpx2024 (km)
20QT20-3	Puruo Gangri	Granite	2.7 ± 1.1	5.2 ± 1.1 (3.2 ± 1.5)	2.9 ± 0.9				
20QT33-4	Puruo Gangri	Granite	1.7 ± 1.6	4.8 ± 1.6 (3.0 ± 1.2)	1.9 ± 0.7				
20QT33-6	Puruo Gangri	Granite	3.7 ± 1.2	5.7 ± 1.2 (3.0 ± 1.3)	2.0 ± 0.6				
21QT77-6	Geladandong	Granite	3.0 ± 1.0	5.3 ± 1.0 (3.4 ± 2.0)	1.6 ± 0.8 (2.8 ± 1.2)				
21QT82-1	Qoima Co	Syenite porphyry	13.3 ± 1.7	10.7 ± 1.7		17.0 ± 7.2	20.2 ± 3.3	14.4 ± 4.5	6.2 ± 2.3
21QT42-4	Meiriqie Co	Granodiorite porphyry				14.7 ± 5.7	12.4 ± 2.6	9.7 ± 3.2	1.5 ± 0.4
21QT59-1	Meiriqie Co	Granodiorite porphyry			4.7 ± 0.9	13.6 ± 5.7	11.9 ± 2.6	9.1 ± 2.9	1.6 ± 0.3
21QT84-4	Maliaoshan	Diorite porphyry	26.9 ± 0.8	20.9 ± 1.0	5.1 ± 0.9				

Note: Hb1992—Al-in-hornblende geobarometer of Schmidt (1992); Hb2016—Al-in-hornblende geobarometer of Mutch et al. (2016); Bt2007—Al-in-biotite barometer of Uchida et al. (2007); Cpx2008—Clinopyroxene barometer of Putirka (2008); Cpx2021—Clinopyroxene barometer of Wang et al. (2021); Cpx2022—Clinopyroxene barometer of Higgins et al. (2022); Cpx2024—Clinopyroxene barometer of Ágreda-López et al. (2024).

† The depth indicated in parentheses is calculated using actinolite.

‡ The depth indicated in parentheses is calculated using biotite inclusions, and the depth for sample 21QT84-4 is calculated using biotite in the matrix.